TAMPEREEN TEKNILLINEN YLIOPISTO
TAMPERE UNIVERSITY OF TECHNOLOGY
Julkaisu 774 • Publication 774

Sami Kujala

Optical Second-harmonic Generation from Metal Nanostructures

Tampere 2008

Tampereen teknillinen yliopisto. Julkaisu 774
Tampere University of Technology. Publication 774

Sami Kujala

Optical Second-harmonic Generation from Metal Nanostructures

Thesis for the degree of Doctor of Technology to be presented with due permission for public examination and criticism in Sähkötalo Building, Auditorium S2, at Tampere University of Technology, on the 28th of November 2008, at 12 noon.

Tampereen teknillinen yliopisto - Tampere University of Technology
Tampere 2008

ISBN 978-952-15-2070-9 (printed)
ISBN 978-952-15-2194-2 (PDF)
ISSN 1459-2045

To my family

Abstract

In this work, we study the second-order nonlinear optical properties of regular arrays of L-shaped gold nanoparticles supported by a substrate. The second-order responses of the samples are shown to depend sensitively on the detailed structure of the samples, which gives rise to interesting and complicated effects in the nonlinear responses, which have not been considered before. The nonlinear measurements are complemented by polarization-dependent linear measurements. In particular, we will show that the sensitivity of second-order processes to symmetry provides important information about the role of structural defects in the nonlinear properties of the structures.

Simple polarized spectral transmission studies in conjunction with second-harmonic generation experiments indicate that the second-harmonic generation from the samples is enhanced by plasmon resonances of the metal particles. Furthermore, these resonances, and thereby second-harmonic generation can be tuned with particle size, shape, and their arrangement in the array. More detailed polarization studies reveal that the certain details of the responses are due to defects of the samples. These defects may give rise to symmetry breaking and that way render ideally symmetric structures chiral. To study the role of these defects in detail, a simple scattering-matrix type formalism is developed to express the tensorial nature of the nonlinear optical process. By relying on the transformation properties of the few lowest order multipoles, their importance to the optical response can be quantified. A symmetry-forbidden tensor component is found to dominate the magnitude of the response and moreover, this component has a strong multipolar character. A simple model is built to explain this behavior. The model assumes that the symmetry is broken by surface defects on the nanoparticles. These defects give rise to the effective dipoles and quadrupoles in the total second-harmonic signal from that particular nanoparticle.

Preface

This research was carried out in the Optics Laboratory of the Tampere University of Finland during the years 2002–2008. I gratefully acknowledge the Graduate School of the Tampere University of Technology, the Academy of Finland and the Nanophotonics Research and Development Program of the Ministry of Education of Finland for funding this work.

The guidance and encouragement of both Professor Martti Kauranen and Dr. Brian K. Canfield has proved to have been an invaluable asset in finishing this work. Without you, things would be very different now. I wish to express my sincerest gratitude for all your efforts.

My sincerest gratitude goes also to our collaborators and co-authors at the University of Joensuu, Professors Jari Turunen and Yuri Svirko, and Dr. Konstantins Jefimovs. Without your efforts, this work would not have been possible.

I would also like to acknowledge my former and current coworkers in the Optics Laboratory. I specially acknowledge (in alphabetical order) Albert, Arri, Iita, Inkeri, Mikael, Mikko, Miro, and Stefano for making me grow into the person I am now.

Second to last, I want to thank my parents, sisters and friends for being there when I needed you. Last, but not least, my love to my wife Mia and my son Aapo for being the beacons to home in on.

Tampere, November 2008

Sami Kujala

Contents

List of Figures

List of Tables

List of Symbols

THG	Third-harmonic generation
CDR	Circular-difference response
EBL	Electron-beam lithography
LHC	Left-hand circular polarization
NRT	Nonlinear response tensor
PAR	Polarization azimuth rotation
PMMA	Poly(methyl methacrylate)
SERS	Surface-enhanced raman scattering
TE	Transverse electric
TM	Transverse magnetic
RHC	Right-hand circular polarization
SHG	Second-harmonic generation
γ	Characteristic collision frequency of free electron gas
Φ	Scalar potential
ρ	Charge density
$\boldsymbol{Q}$	Quadrupole moment
$\boldsymbol{B}$	Magnetic-flux density
$\boldsymbol{D}$	Electric displacement
$\boldsymbol{E}$	Electric field
$\boldsymbol{H}$	Magnetic field
$\boldsymbol{J}$	Current density
$\boldsymbol{M}$	Magnetization
$\boldsymbol{m}$	Magnetic dipole moment
$\boldsymbol{P}$	Electric polarization
$\boldsymbol{p}$	Dipole moment
d	Nanoparticle array period

k	Wave number
L	Nanoparticle arm length
q	Total charge
T	Transmissivity

List of Publications

Paper 1 B. K. Canfield, S. Kujala, K. Jefimovs, T. Vallius, J. Turunen, and M. Kauranen. Linear and Nonlinear Optical Responses Influenced by Broken Symmetry in an Array of Gold Nanoparticles. Opt. Express, **12**, 5418 (2004).

Paper 2 B. K. Canfield, S. Kujala, K. Jefimovs, T. Vallius, J. Turunen, and M. Kauranen. Polarization Effects in the Linear and Nonlinear Optical Responses of Metal Nanoparticle Arrays. J. Opt. A: Pure Appl. Opt, **7**, S110 (2005).

Paper 3 B. K. Canfield, S. Kujala, K. Laiho, K. Jefimovs, J. Turunen, and M. Kauranen. Chirality arising from small defects in gold nanoparticle arrays. Opt. Express, **14**, 950 (2006).

Paper 4 B. K. Canfield, S. Kujala, K. Jefimovs, Y. Svirko, J. Turunen, and M. Kauranen. A macroscopic formalism to describe the second-order nonlinear optical response of nanostructures. J. Opt. A: Pure Appl. Opt, **8**, S278 (2006).

Paper 5 S. Kujala, B. K. Canfield, M. Kauranen, Y. Svirko, and J. Turunen. Multipole Interference in the Second-Harmonic Optical Radiation from Gold Nanoparticles. Phys. Rev. Lett., **98**, 167403 (2007). Featured in April 30, 2007 issue of Virtual Journal of Nanoscale Science & Technology **15**, (2007).

Paper 6 S. Kujala, B. K. Canfield, M. Kauranen, Y. Svirko, and J. Turunen. Multipolar analysis of second-harmonic radiation from gold nanoparticles. Opt. Express, **16**, 17196 (2008).

Author's Contribution

The subject of the articles included in this thesis and their key results are listed below.

Paper 1 This paper presents results of linear and nonlinear measurements on an array of low-symmetry, L-shaped gold nanoparticles. We show that the optical responses are very sensitive to the polarization of the exciting beam as a result of nonidealities in particle shape. Nonlinear experiments reveal strong signals from disallowed polarization combinations.

Paper 2 In a collection of linear and nonlinear experiments, we find the responses of nanostructure arrays to be exceptionally sensitive to polarization. This sensitivity is determined to arise from overall structural properties of the particles. Nonlinear polarization measurements yield surprising information concerning the symmetry of the nanoparticle arrays. The results lead us to conclude that it is the smallest details of the arrays that influence optical responses.

Paper 3 This paper discusses two possible mechanisms of breaking the symmetry in metal nanostructures: structural features and small-scale defects. For this purpose, nanostructures were prepared to exhibit broken symmetry on different levels. Linear optical measurements are somewhat inconclusive on the effect of symmetry-breaking, whereas for second-harmonic generation the effects are enormous. The responses of all structures are very similar, which suggests that uncontrollable defects have an important role in symmetry breaking.

Paper 4 We develop a scattering matrix like formalism called nonlinear response tensor (NRT) to describe second-order nonlinear optical responses of our nanostructures. This formalism neglects the fine details about the electromagnetic field distribution and material inhomogeneities in the structures and the complicated interactions and interferences occurring on the nanoscale and focuses on the measurable macroscopic input / output polarization combinations.

Paper 5 In an application of the NRT formalism, we provide evidence of higher multipoles in the second-harmonic radiation from arrays of metal nanoparticles. The analysis is based on the fundamental differences in the radiative properties of different multipolar orders. We estimate that higher multipoles contribute up to 20% of the total emitted SH field amplitude for certain polarization configurations.

Paper 6 We present a multipolar tensor analysis of second-harmonic radiation from arrays of gold nanoparticles. We find the nonlinear response to be dominated by a tensor component, not resolved in **Paper 5**, which is associated with chiral symmetry breaking and which also contains a strong multipolar contribution. The results suggest that the multipolar contribution exhibits a quadrupolar character arising from retarded second-harmonic emission from asymmetrical defects on opposite sides of the particles.

Science is, and should always be, not result of one man's sole effort but rather, the result of collaborative team effort. The author's contribution to each of the included publications is shown in Table 1. The contribution percentages are divided into three categories; "Preparation", "Experiments", and "Reporting". Preparation consists of the design and evaluation of the experimental method, experiments includes the implementation of the experimental method and performing the actual measurement, and finally reporting contains the analysis of the experimental data as well as preparation and revising the manuscript.

Table 1. Summary of author's contribution to articles included in this thesis.

Paper	Preparation	Experiments	Reporting
Paper 1	20 %	60 %	20 %
Paper 2	50 %	70 %	50 %
Paper 3	30 %	60 %	20 %
Paper 4	50 %	100 %	40 %
Paper 5	80 %	100 %	90 %
Paper 6	90 %	100 %	90 %

Related Publications with Author's Contribution

RP1 B. K. Canfield, S. Kujala, K. Jefimovs, T. Vallius, J. Turunen, and M. Kauranen. Remarkable Polarization Sensitivity of Gold Nanoparticle Arrays. Appl. Phys. Lett., **86**, 183109 (2005).

RP2 B. K. Canfield, S. Kujala, K. Laiho, K. Jefimovs, T. Vallius, J. Turunen, and M. Kauranen. Linear and Nonlinear Optical Properties of Gold Nanoparticles with Broken Symmetry. J. Nonlinear Opt. Phys. Mat., **15**, 43 (2006).

RP3 B. K. Canfield, S. Kujala, H. Husu, M. Kauranen, B. Bai, J. Laukkanen, M. Kuittinen, Y. Svirko, and J. Turunen. Local-Field and Multipolar Effects in the Second-Harmonic Response of Arrays of Metal Nanoparticles. J. Nonlinear Opt. Phys. Mat., **16**, 317 (2007).

Peer-reviewed Conference Proceedings

CP1 B. K. Canfield, S. Kujala, K. Jefimovs, T. Vallius, J. Turunen, and M. Kauranen. Exceptional Linear and Nonlinear Optical Properties of Low-Symmetry Metal Nanoparticle Arrays. In N. J. Halas and T. R. Huser, eds., *Plasmonics: Metallic Nanostructures and Their Optical Properties II*, volume 5512 of *Proc. SPIE*, 107–116 (2004).

CP2 B. K. Canfield, S. Kujala, M. Kauranen, K. Jefimovs, T. Vallius, and J. Turunen. Extraordinary Polarization Sensitivity of Nanoparticle Arrays to Structural Asymmetry. In *Conference on Lasers and Electro-Optics/International Quantum Electronics Conference*, paper IWG6 (Optical Society of America, Washington, DC, 2004).

CP3 S. Kujala, B. K. Canfield, M. Kauranen, K. Jefimovs, and J. Turunen. Effects of Polarization and Grating Period on Second-Harmonic Generation from Arrays of Anisotropic Gold Nanoparticles. In *Conference on Lasers and Electro-Optics/International Quantum Electronics Conference*, paper IFE1 (Optical Society of America, Washington, DC, 2004).

CP4 S. Kujala, B. K. Canfield, M. Kauranen, K. Jefimovs, and J. Turunen. Effects of Polarization and Grating Period on Second-Harmonic Generation from Arrays of Anisotropic Gold Nanoparticles. In *Proceedings of the XXXVIII Annual Conference of the Finnish Physical Society*, 293 (University of Oulu, Oulu, 2004).

CP5 B. K. Canfield, S. Kujala, K. Laiho, M. Kauranen, K. Jefimovs, and J. Turunen. Robust Nonlinear Chiral Responses from Gold Nanoparticle Arrays. In *Conference on Lasers and Electro-Optics/International Quantum Electronics Conference and Photonic Applications, Systems and Technologies 2005*, paper QMH5 (Optical Society of America, Washington, DC, 2005).

CP6 B. K. Canfield, S. Kujala, K. Laiho, H. Husu, K. Jefimovs, Y. Svirko, J. Turunen, and M. Kauranen. Second-order optical characterization of

gold nanoparticle arrays. In D. L. Andrews, J.-M. Nunzi, and A. Ostendorf, eds., *SPIE Photonics Europe*, volume 6195 of *Nanophotonics*, 619503 (SPIE, Bellingham, WA, 2006).

CP7 B. K. Canfield, S. Kujala, K. Jefimovs, Y. Svirko, J. Turunen, and M. Kauranen. The role of multipole contributions to the second-order response of gold nanoparticles. In M. I. Stockman, ed., *Plasmonics: Metallic Nanostructures and Their Optical Properties IV*, volume 6323 of *Plasmonics: Metallic Nanostructures and their Optical Properties IV*, 63230T (SPIE, Bellingham, WA, 2006).

CP8 S. Kujala, B. K. Canfield, M. Kauranen, K. Jefimovs, and J. Turunen. Tensorial second-order nonlinear optical responses of arrays of gold nanoparticles. In M. Kauranen, A. Laitinen, J. Nieminen, and T. T. Rantala, eds., *Proceedings of the XL Annual Conference of the Finnish Physical Society*, Institute of Physics, Report 2006:1, 294 (Tampere University of Technology, Institute of Physics, 2006).

CP9 S. Kujala, B. K. Canfield, M. Kauranen, Y. Svirko, and J. Turunen. Multipolar tensor analysis of second-harmonic radiation from gold nanoparticles. In M. I. Stockman, ed., *Plasmonics: Metallic Nanostructures and Their Optical Properties VI*, volume 7032, 70321Y (2008).

1 Introduction

Metal nanostructures in various forms have drawn the interest of mankind for more than a millennium. Already in the Ancient Roman times, colloidal metal was used to produce very intense shades in glass-coloring. Colloidal gold consists of nanoscopic gold particles, often in a liquid suspension, but the particles can also be embedded in a solid matrix or on top of solid substrates. The color of such samples depends on the size (distribution) and chemical composition of the nanoparticles in question[7]. In the recent years, scientific interest in metal nanoparticles has given birth to the new research field of *nanoplasmonics*, which is increasing very rapidly and is believed to lead to new materials whose optical properties can be engineered for various applications.

1.1 Aim and Scope of This Work

This research began originally in the year 2001* with several ideas and many open questions. The purpose of the work is to study the nonlinear optical properties of metal nanoparticles, in order to gain understanding of the underlying physical processes. Obtaining this understanding is crucial, as the most interesting – and challenging – fact related to nanostructures is that they fall somewhere in between the quantum realm and the macroscopic domain. They are far too large to be explained quantum-mechanically and small enough so that their material properties depend not only on the material and optical frequency, but also on the size and shape of these structures. It is, however, common to try to describe the material properties by the bulk dielectric constant. Even then, the optical responses are found to depend sensitively on the size and shape of the particles.

In this work, we will be particularly interested in the second-order nonlinear optical properties of regular arrays of metal nanoparticles supported by a substrate. The second-order responses depend sensitively on the structural symmetry of the samples, which can give rise to interesting polarization dependences in the responses. The nonlinear measurements are complemented by polarization-dependent linear measurements. This limit in scope is, in fact, not as severe as one might casually think and we will provide evidence of a rich variety of effects that have not been previously observed. In particular, we will show that the sensitivity of second-order

*The author joined the research group in 2002

processes to symmetry provides important information about the role of structural defects in the nonlinear properties of the structures.

1.2 Structure of the Thesis

This Thesis is divided into a summary and overview of the research, which are followed by six original publications. Chapter 2 describes the very basic notions of nonlinear optics, deriving the wave equation for nonlinear polarization from the Maxwell equations and constitutive relations. We next introduce some of the nonlinear optical phenomena and finally conclude with a discussion of the various symmetry arguments related to second-order nonlinear responses.

In Chapter 3, we discuss the physical origins related to the optical responses of metal nanostructures, the plasmons. After building the basic understanding of plasmonic effects, we conclude the chapter with a review of related literature and recent work done by other research groups.

The multipole expansion of the light-matter interaction is introduced in Chapter 4. We begin by studying simple static electric and magnetic fields, and then generalize the discussion to the multipole expansion of radiating sources. We next discuss the implications of the multipole expansion in two applications: the scattering theory of Mie and the microscopic light-matter interaction Hamiltonian. Finally we introduce an experimental way of separating the first few multipolar orders in the second-harmonic responses of our samples. We also develop a phenomenological model of effective quadrupoles to interpret the origins of our findings.

The experimental procedures used to determine the optical properties of our samples are depicted in Chapter 5. The results obtained from the experiments and published in the original publications are summarized in Chapter 6. Final concluding remarks are given in Chapter 7.

2 Fundamentals of Nonlinear Optics

> "Physics would be dull and life most unfulfilling if all physical phenomena around us were linear. Fortunately, we are living in a nonlinear world. While linearization beautifies physics, nonlinearity provides excitement in physics."[8]

2.1 Maxwell Equations in Nonlinear Media

The physical laws governing all classical electromagnetism can be summarized into the famous Maxwell equations, given in differential form and SI units as[9]

$$\begin{aligned} \nabla \cdot \boldsymbol{D} &= \rho, & \nabla \times \boldsymbol{E} &= -\frac{\partial \boldsymbol{B}}{\partial t}, \\ \nabla \cdot \boldsymbol{B} &= 0, \quad \text{and} & \nabla \times \boldsymbol{H} &= \boldsymbol{J} + \frac{\partial \boldsymbol{D}}{\partial t}, \end{aligned} \tag{2.1}$$

where the electric quantities $\boldsymbol{E}$ and $\boldsymbol{D}$ are the electric field and the electric displacement, respectively. The magnetic quantities $\boldsymbol{B}$, $\boldsymbol{H}$ are the magnetic-flux density and the magnetic field, respectively. The quantities related to the medium itself are the free charge density ρ and the free current density $\boldsymbol{J}$. Note that a material, e.g., a metal can support free currents, even if it is electrically neutral, i.e., there is no excess free charge.

These equations, coupled with the constitutive equations describing the medium,

$$\boldsymbol{D} = \epsilon_0 \boldsymbol{E} + \boldsymbol{P} \quad \text{and} \quad \boldsymbol{H} = \frac{1}{\mu_0}\boldsymbol{B} - \boldsymbol{M}, \tag{2.2}$$

give a complete description for classical light-matter interactions. The quantities $\boldsymbol{P}$, electric polarization, and $\boldsymbol{M}$, magnetization, describe the material response to external electro-magnetic perturbations.

Now, taking the curl of $\nabla \times \boldsymbol{E}$ and combining equations from Eq. (2.1) and (2.2) yields in the plane-wave approximation where $\nabla \cdot \boldsymbol{E} \equiv 0$

$$\nabla^2 \boldsymbol{E} - \frac{1}{c^2}\frac{\partial^2 \boldsymbol{E}}{\partial t^2} = \frac{\partial}{\partial t}\left(\mu_0 \boldsymbol{J} + \nabla \times \boldsymbol{M}\right) + \mu_0 \frac{\partial^2 \boldsymbol{P}}{\partial t^2}, \tag{2.3}$$

which is an inhomogeneous wave equation with the electric polarization $\boldsymbol{P}$, the magnetization $\boldsymbol{M}$, and the current density $\boldsymbol{J}$ as its source terms. Unfortunately, there is no generally valid expression between the fields and sources. However, the current density $\boldsymbol{J}$ can be shown to act via conductivity as a source that gives rise to losses. In addition, the various multipolar currents can therefore be absorbed in the other respective sources. This leads to the expansion of the source in terms of its multipolar orders[10]

$$\nabla^2\boldsymbol{E} - \frac{1}{c^2}\frac{\partial^2\boldsymbol{E}}{\partial t^2} = \nabla \times \frac{\partial}{\partial t}\Big[\boldsymbol{M}_d + \ldots\Big] + \mu_0 \frac{\partial^2}{\partial t^2}\Big[\boldsymbol{P}_d + \nabla\cdot\boldsymbol{Q} + \ldots\Big] \tag{2.4}$$

where the new quantities $\boldsymbol{M}_d$, $\boldsymbol{P}_d$, and $\boldsymbol{Q}$ are dipolar magnetization, dipolar electric polarization, and electric quadrupolarization, respectively. This expansion is useful to approximate the spatial variations of polarization and magnetization.

The multipole expansion will be discussed in more detail in Section 4.2, but for the purposes of the current introductory discussion we retain only the electric polarization, $\boldsymbol{P}_d$ obtaining finally

$$\nabla^2\boldsymbol{E} - \frac{1}{c^2}\frac{\partial^2\boldsymbol{E}}{\partial t^2} = \mu_0 \frac{\partial^2\boldsymbol{P}_d}{\partial^2 t}, \tag{2.5}$$

which is a wave equation for $\boldsymbol{E}$ driven by the electric dipole source polarization, which includes the contribution of dipolar currents also. Henceforth, unless otherwise noted, we focus the discussion on the electric dipole polarization only and drop the subscript d in Eq. (2.5).

We next consider the temporal behavior of the polarization. Since we are interested in studying effects induced by light, we expand the time-dependence of the electric dipole polarization $\boldsymbol{P}$ as power series of time-dependent excitation $\boldsymbol{E}_i$ and then decompose the unknown time-dependence via Fourier expansion into a superposition of time-harmonic oscillation at frequencies ω_n. The Fourier components for both the field and polarization are thus of the form

$$\boldsymbol{F}(t) = \boldsymbol{F}(\omega)\,\mathrm{e}^{-i\omega t} + \boldsymbol{F}^*(\omega)\,\mathrm{e}^{i\omega t}, \tag{2.6}$$

where the asterisk ($*$) refers to complex conjugation, and negative frequencies are connected with the complex conjugate $\boldsymbol{F}^*$.

The linearity of Maxwell's equations (and the resulting partial differential equations)

allows each frequency component to be handled separately. Therefore we obtain

$$\begin{aligned}
\boldsymbol{P}(\omega) &= \epsilon_0 \chi^{(1)}(\omega) \cdot \boldsymbol{E}(\omega_1) && \text{(2.7a)}\\
&\quad + \epsilon_0 \boldsymbol{\chi}^{(2)}(\omega = \omega_1 + \omega_2) : \boldsymbol{E}(\omega_1)\boldsymbol{E}(\omega_2) && \text{(2.7b)}\\
&\quad + \epsilon_0 \boldsymbol{\chi}^{(3)}(\omega = \omega_1 + \omega_2 + \omega_3) \vdots \boldsymbol{E}(\omega_1)\boldsymbol{E}(\omega_2)\boldsymbol{E}(\omega_3) && \text{(2.7c)}\\
&\quad + \cdots \\
&= \boldsymbol{P}^{(1)}(\omega) + \boldsymbol{P}^{(2)}(\omega) + \boldsymbol{P}^{(3)}(\omega) + \cdots .
\end{aligned}$$

where $\boldsymbol{P}^{(n)}$ is the nth-order electric-dipole polarization. Eq. (2.7) may be grouped into two parts, one describing the linear response and the other describing the nonlinear response, as follows:

$$\begin{aligned}
\boldsymbol{P}(\omega) &= \boldsymbol{P}^{\mathrm{L}}(\omega) + \boldsymbol{P}^{\mathrm{NL}}(\omega); && \text{(2.8)}\\
\boldsymbol{P}^{\mathrm{L}}(\omega) &= \boldsymbol{P}^{(1)}(\omega), && \text{(2.9)}\\
\boldsymbol{P}^{\mathrm{NL}}(\omega) &= \sum_{n>1} \boldsymbol{P}^{(n)}(\omega). && \text{(2.10)}
\end{aligned}$$

Therefore, the wave equation (2.5) becomes

$$\nabla^2 \boldsymbol{E}(\omega) + \frac{\omega^2 \boldsymbol{\epsilon}(\omega)}{c^2} \boldsymbol{E}(\omega) = \frac{\omega^2}{c^2} \boldsymbol{P}^{\mathrm{NL}}(\omega), \tag{2.11}$$

where $\boldsymbol{\epsilon} = 1 + \boldsymbol{\chi}^{(1)}$ is the linear permittivity (dielectric constant) of the medium. This equation thus describes the wave that will be generated from the nonlinear source polarization.

2.2 Nonlinear Optical Effects

Let us consider Eq. (2.7) more closely. As an example, consider the term (2.7b). The terms clearly represent an interaction which combines two electric fields, $\boldsymbol{E}(\omega_1)$ and $\boldsymbol{E}(\omega_2)$, at potentially different frequencies. This interaction produces polarization in the medium which oscillates at a third frequency. This polarization, coupled into Eq. (2.11), acts as a source to oscillating electric field at this new frequency.

To illustrate the notion of frequency conversion, consider two waves at frequencies ω_1 and ω_2. The second-order nonlinear interaction in Eq. (2.7b) combines these two fields to produce a new field at a different frequency. As the Fourier-transform introduced in Eq. (2.7) allows negative frequency arguments for the fields and susceptibil-

ities, the interaction of the two fields produces *three* new frequencies:

$$\boldsymbol{P}(\omega_1 + \omega_2) = \chi^{(2)} : \boldsymbol{E}(\omega_1)\boldsymbol{E}(\omega_2) \tag{2.12}$$

$$\boldsymbol{P}(\omega_1 - \omega_2) = \chi^{(2)} : \boldsymbol{E}(\omega_1)\boldsymbol{E}(-\omega_2) \tag{2.13}$$

$$\boldsymbol{P}(\omega_2 - \omega_1) = \chi^{(2)} : \boldsymbol{E}(-\omega_1)\boldsymbol{E}(\omega_2) \tag{2.14}$$

These effects are known as the *sum-* and *difference-frequency generation*. When the frequencies ω_1 and ω_2 are the same, ω, the effects become the *second-harmonic generation* (SHG)nd *optical rectification*, respectively.

For the third-order nonlinear interaction, Eq. (2.7c), the multitude of phenomena is even more complicated. For example, these processes include *third-harmonic generation* (THG) The third-order effects also include effects where the frequencies of the field do not change and thus can also influence the interacting fields themselves through the nonlinear polarization. As an example, in *cross-phase modulation* the electric field $\boldsymbol{E}(\omega_1)$ changes the refractive index experienced by the field $\boldsymbol{E}(\omega_2)$. The change in the refractive index depends on the amplitude of $\boldsymbol{E}(\omega_1)$. In *self-phase modulation* and *self-focusing* processes the $\boldsymbol{E}(\omega_1)$ changes its own refractive index through the third-order polarization[11]. The third-order effects can be especially important in fiber-optical applications where the interaction lenghts are long and the amplitude of the field(s) can be high due to strong confinement of light within the fiber core[12].

2.3 The Effect of Symmetry in Nonlinear Optics

The effects described in the previous section are the result of tensorial interaction of multiple electric fields. The tensorial interaction dictates that the vectorial nature of the fields may not be neglected. Moreover, the symmetry properties of the $\chi^{(n)}$ tensor are of great importance. For simplicity, we will henceforth concentrate on second-order effects only, but similar arguments can be applied to higher-order effects as well.

Permutation symmetries

Intrinsic permutation symmetry arises from the arbitrariness of the order of the fields in performing the contraction in Eq. (2.7b). It tells us that in the expression for $\chi^{(2)}_{ijk}$ we may interchange the last two indices, provided we interchange the last two frequency arguments at the same time:

$$\chi^{(2)}_{ijk}(\omega_n + \omega_m; \omega_n, \omega_m) = \chi^{(2)}_{ikj}(\omega_n + \omega_m; \omega_m, \omega_n). \tag{2.15}$$

Two more symmetries apply when the material is lossless. First, components of $\boldsymbol{\chi}^{(2)}$ are real:

$$\chi^{(2)}_{ijk}(\omega_n + \omega_m; \omega_n, \omega_m) = \chi^{(2)*}_{ijk}(\omega_n + \omega_m; \omega_n, \omega_m). \tag{2.16}$$

Second, the *full permutation symmetry* applies for a medium without losses. It means that all frequency components in $\chi^{(2)}_{ijk}(\omega_\sigma = \omega_n + \omega_m)$ may be permuted freely, provided that the indices i, j, and k are permuted at the same time. Also, it must be remembered that first frequency argument is always the sum of the latter two:

$$\chi^{(2)}_{ijk}(\omega_\sigma = \omega_n + \omega_m; \omega_n, \omega_m) = \chi^{(2)}_{kij}(\omega_m; \omega_\sigma = \omega_n + \omega_m, -\omega_n). \tag{2.17}$$

Now suppose that the frequency dispersion of $\boldsymbol{\chi}^{(2)}$ is negligible. This is the case if all the frequencies involved are much less than the lowest resonance frequency of the medium. The medium is then also necessarily lossless, since the applied frequencies are far from resonance. As a consequence of full permutation symmetry, we may again permute the indices as long as we permute the frequencies as well, but the lack of dispersion implies that the ordering of frequencies in $\chi^{(2)}_{ijk}(\omega_\sigma; \omega_n, \omega_m)$ is irrelevant. Thus, we conclude that we may permute the spatial indices without permuting frequency arguments:

$$\chi^{(2)}_{ijk} = \chi^{(2)}_{ikj} = \chi^{(2)}_{jik} = \chi^{(2)}_{kji} = \chi^{(2)}_{kji} = \chi^{(2)}_{jki}. \tag{2.18}$$

This is the *Kleinman symmetry*. Unfortunately it has only limited validity in practical nonlinear optical applications[13].

Structural symmetry

When the original coordinates describing the nonlinear material, (x, y, z), are transformed into (x', y', z'), the third-rank tensor $\chi^{(2)}_{ijk}$ transforms as follows[14]:

$$\chi^{(2)\prime}_{ijk} = \sum_{mn\sigma} \frac{\partial x'_i}{\partial x_m} \frac{\partial x'_j}{\partial x_n} \frac{\partial x'_k}{\partial x_\sigma} \chi^{(2)}_{mn\sigma}. \tag{2.19}$$

If the coordinate transformation is also a symmetry operation of the material, both the transformed $\chi^{(2)\prime}_{ijk}$, and the original $\chi^{(2)}_{ijk}$ must be equal.

Arguments based on spatial symmetry of the material are particularly important as they can be used to significantly reduce the number of independent nonvanishing tensor components. On the other hand, the structure of an experimentally determined tensor provides important information on the structural symmetry of the sample investigated[15].

Detailed measurements of the tensorial nonlinear response are an essential part of this thesis. However, as explained in Section 4.5, we use a slightly modified formalism from the above to discuss the symmetry issues, which is better adapted to describe the nonlinear properties of nanostructures.

The nonlinear optical response of a material system may include contributions beyond the electric-dipole interaction, for example magnetic-dipole or electric-quadrupole interactions. Traditionally these processes are described in the framework of susceptibility tensor formalism by defining additional susceptibility tensors that relate the interactions through multipoles *at the fundamental wavelength* or by susceptibility tensors which give rise to higher multipole sources, such as magnetization or quadrupolarization, see Eq. (2.11) and, e.g., Refs. [16,17]. These interactions will be discussed in the context of the multipole expansion in Section 4.3.

Usually, any symmetry arguments are based on the structural properties of the susceptibility tensors. In this work, an important additional benefit is achieved by using an experimental geometry where the sample and tensors arising from the formalism in Paper 4 are described in the same coordinate system. The relative importance of the various symmetry elements in any given signal can then be determined using only electric-dipole-type selection rules even though higher multipole interactions may play an important role in the nonlinear response.

3 Metal Nanostructures

In this chapter, we introduce the basic principles behind the optical response of metal nanostructures. We begin by describing a simple phenomenological model for the dielectric function of free-electron gas. This simple model predicts the wavelength-dispersion of the dielectric function surprisingly well – provided that we stay at longer wavelengths than the interband transitions of the metal. We continue with a discussion of plasmonic excitations in metals and conclude with a review into current nanoparticle research.

3.1 Drude Model for Permittivity of Free-electron Gas

The optical properties of metals can be explained over a wide frequency range by a plasma model, where the conduction electrons move almost freely within the volume of the metal against a background of the positive ion cores. The band structure and the electron-electron interactions are not taken into account in the model. Some of the aspects of the band-structure are lumped into the mass of electrons, which is adjusted into the so-called optical mass [18].

Taking the equation of motion for free electrons driven by the electric field as the starting point, we arrive to the dielectric function ϵ as [18]

$$\begin{aligned} \epsilon &= 1 - \frac{\omega_p^2}{\omega^2 + i\gamma\omega} \\ &= 1 - \frac{\omega_p^2}{\omega(\omega + i\gamma)} \end{aligned} \tag{3.1}$$

where γ is the characteristic collision frequency of the free electron gas, m is the optical mass of the electron and $\omega_p = ne^2/\epsilon_0 m$ is the plasma frequency of the free electron gas, which depends on the density n of electrons in the metal. Typical plasma frequencies of noble metals occur in the range of ultraviolet to visible parts of the electromagnetic spectrum.

The form of the dielectric function has some interesting consequences. For very low frequencies, the dielectric function becomes essentially imaginary, which corresponds to the high conductivity of metals at low frequencies. Although the losses

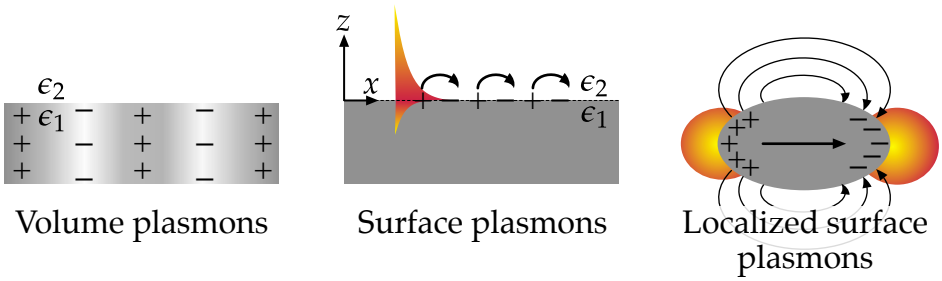

Figure 3.1 Schematic illustration of the three main types of plasmonic excitations that can occur in metals

are high, almost no radiation can penetrate the metal and therefore the reflectivity is high. For very high frequencies, on the other hand, the function approaches unity, which implies high transparency, e.g., in the X-ray regime [19].

Near infrared and optical frequencies are usually lower than the plasma frequency. Assuming that the relaxation rate γ is relatively small, the dielectric function is essentially real but negative. This property is most important and gives rise to the plasmon resonances that dominate the optical response of metal nanostructures.

3.2 Plasmons

In metal structures, the macroscopic optical properties are mainly determined by the response of the conduction electrons of the metal. The electromagnetic excitation causes these electrons to oscillate collectively as plasmons within the confining space of the structure, forming an oscillator system. Depending on the applicable boundary conditions, the plasma oscillations can be categorized into three different modes: volume plasmons, surface plasmons, and localized surface plasmons, schematically illustrated in Fig. 3.1.

Bulk plasmons are collective oscillations of the electron gas in the bulk of the metal, and the energy of their quanta is typically on the order of 10 eV (corresponding to a vacuum wavelength of $\sim$ 120 nm) in noble metals. Bulk plasmons cannot be directly excited with electromagnetic radiation, because of their longitudinal nature. The bulk plasmons are usually studied experimentally using electron loss spectroscopy [18,20].

Surface plasmons occur at metal-dielectric interfaces, where the longitudinal charge density oscillations propagate along the interface as "polarization waves". When we consider waves that propagate along the surface in the x-direction (cf. Fig. 3.1), we find that the wave equation [Eq. (2.11)] yields two possible modes of propagating waves. These modes are the transverse magnetic (TM) and the transverse electric (TE)

modes. The boundary conditions between the two media dictate that only TM modes may excite surface plasmons, and moreover, only such TM modes can propagate that fulfill the dispersion relation

$$k_x = \frac{\omega}{c}\sqrt{\frac{\epsilon_1\epsilon_2}{\epsilon_1+\epsilon_2}}, \tag{3.2}$$

where k_x is the component of the wavevector along the propagation direction of the plasmon wave, and ϵ_1 and ϵ_2 are the dielectric constants of the metal and the surrounding dielectric, respectively. A direct consequence of the dispersion relation is that the real part of ϵ_1 needs to be negative, which is satisfied with noble metals in the visible to near infrared spectral regions for instance. Therefore the electric fields outside the metal become

$$E_x = iE_0\frac{1}{\omega\epsilon_0\epsilon_2}k_z e^{ik_x x}e^{-k_z z} \tag{3.3}$$

$$E_z = -E_0\frac{k_x}{\omega\epsilon_0\epsilon_2}k_z e^{ik_x x}e^{-k_z z}. \tag{3.4}$$

Equations (3.3) and (3.4) correspond to waves which decay exponentially perpendicular to the surface. The dispersion relation [Eq. (3.2)] implies that surface plasmons have a longer wave vector than photons at the same energy, $k_x > \omega/c = k_0$. Therefore, surface plasmons cannot be excited with light propagating in free space. There are a few methods to account for the wave vector mismatch. One such method is grating coupling[20], where the surface is modified with a periodic lattice. This modification provides for the missing wavevector.

When the plasma oscillations are confined in all three spatial dimensions, as is the case in, e.g., metal nanostructures, the oscillation mode is called localized surface plasmon (see, e.g., Refs. [18,21]). In this mode, the conduction electrons oscillate within the particle and form an oscillator system with resonance behaviour. Particle plasmons can be excited by light propagating in free space.

Localized surface plasmons turn the electromagnetic problem into a scattering problem. Analytical solutions to the problem are unfortunately limited to spheres, ellipsoids and spheroids[7,18,22]. An approximate optical response can be obtained in the *quasi-static regime* where the particle size is small compared to wavelength. Within the quasi-static regime the retardation effects of the exciting electric field across the particle are neglected and the field distribution is obtained using electrostatic arguments[7,22]. To go beyond the electrostatic approximation, a more rigorous electrodynamic discussion is required. Gustav Mie was the first to explain the optical responses of nanoscopic spherical particles with his theory[23] in 1908. His theory solves the Maxwell equations exactly while the fundamental light-matter interaction

is embedded in an experimentally obtained or phenomenologically derived dielectric function, such as the Drude function. The Mie theory will be discussed in more detail in terms of multipoles in Section 4.3.

Local-field Enhancement

As we saw already in equations (3.3) and (3.4), the exponential decay in the z-direction (surface normal), implies that there is a strong concentration of electromagnetic energy within the $1/|k_{z,i}|$ distance from the surface. Moreover, this localization is directly dependent on the dielectric constants ϵ_1 and ϵ_2 as[20]

$$\frac{1}{|k_{z,2}|} = \frac{1}{k_0}\sqrt{\frac{\mathrm{Re}\,\epsilon_1 + \epsilon_2}{\epsilon_2^2}}. \tag{3.5}$$

Similar arguments apply to localized surface plamons, or particle plasmons for short. Moreover, to satisfy the momentum conservation, the tangential component of electric (and magnetic) field is continuous across the interface between the surrounding medium[24], which means that the electric field attempts to remain perpendicular to the surface*. If the material has areas where the local radii of curvature of the material are small (sharp tips etc.), this kind of behaviour results in the concentration of the electromagnetic field (and thereby energy) in these pointed areas. This effect is known as the *lightning rod effect*. The lightning rod effect is one of the dominating effects in producing the local-field enhancements in metal nanostructures[25]. The local-field often localizes strongly into so called "hot spots", where the field strength can be orders of magnitude larger than the applied external field[26].

3.3 Review into Nanoparticle Research

The scientific interest in the optical properties of nanoscopic particles has been steadily increasing. What makes them particularly interesting is that they fall in somewhere between the quantum realm and bulk matter domain. As the particles sizes approach the skin-depth of the metals ($\sim 20 - 30$ nm), simple arguments of down-scaling bulk material properties fail to provide adequate description of the optical properties[27]. Moreover, diffraction imposes difficulties in confining light into small space. These difficulties are particularly challenging in, e.g., antenna applications where the attempt is to couple optical radiation into small, sub-micron volumes. In the following, we present a non-exhaustive overview of recent related work in the field of optics of

*This is strictly true only when the metal is in the near-perfect conductor regime

nanoparticles and -structures.

Surface-enhanced Raman Scattering

Raman scattering is an inelastic scattering process, where the wavelength of the scattered light changes. During the scattering process, some of the incident photon energy is absorbed into the molecule and therefore the scattered photon has lower energy. The energy absorbed by the molecule may appear as vibrational, rotational, or electronic energy of the molecule. The incident photon may also scatter from a vibrationally excited molecule, de-exciting the molecule and thus gaining energy in the process. This is called the anti-Stokes radiation, in contrast to Stokes radiation, where some of the incident photon energy is lost[28].

Absorption and re-emission of the incident photons depend on the local field at the Raman-active molecule. Strong local fields enhance the Raman process by increasing the effective Raman cross section. This enhancement is mainly due to electric and chemical (resonant charge transfer) mechanisms. The presence of metal nanoparticles on a surface loaded with Raman-active molecules provides conveniently the strong local fields due to field localization at the metal particles. This surface geometry is traditionally called surface-enhanced Raman Scattering (SERS). SERS was observed for the first time in 1974 on roughened silver surfaces[29]. During the following years, the presence of noble metals on surfaces was reported to enhance the Raman scattering and fluorescence efficiency by many orders of magnitude (see e.g., Refs. [30–32] and references therein).

As the frequency shifts related to Raman scattering are small, the effective Raman cross sections for both absorption and emission can be enhanced at the same site, which may lead to very large enhancement factors, up to 13 orders of magnitude[33]. The large enhancement factors are very beneficial for sensitive measurements and in fact, SERS has also been successfully used for single-molecule detection[31,32,34,35].

Usually, the metal structures which are used to enhance SERS are essentially random structures, like roughened surfaces[36–38]. However, the arrangement of nanoparticles used to localize fields has drawn attention, and attempts to optimize the resonance conditions leading to local field enhancements and thereby enhancement of SERS have been made. For example, the enhancement of SERS has been studied on tunable nanogaps[39], nanoshells[40], pits in regular arrays[41], microstructured optical fibers[42], and self-similar chains of nanoparticles[43].

Nanoantennas

In the past few years, the interest in the optical analogue of radio and microwave antennas has gained much momentum. The research on these "nanoantennas" or "optical antennas" is still in its infancy, though. Nanoantennas are devices designed to provide efficient coupling between near and far fields. As a concrete example, nanoantennas are used as a gateway for coupling electromagnetic energy between macroscopic fields and nanoscale devices, which mainly operate in the near field regime. In this function, they can be also viewed as a kind of nanolens for focusing electromagnetic energy beyond the diffraction limit.

A key concept behind the nanoantennas is the local-field enhancement. Having nanoparticles in close proximity to each other may result in the coupling of their respective plasma oscillations and thereby changing the resonance conditions. This change can also be viewed as plasmon hybridization, that is, the merging of the individual particle plasmons into bonding and antibonding linear combinations of the original plasmons[44]. This model has been used to analyze plasmon hybridization in nanodimers[45], in systems with nanoparticles near metallic surfaces[45] and in nanoshells[46]. This concept is important, as a direct consequence of it is that this change in plasmon resonances can be effectively used to map local fields in surfaces and in nanostructures.

Various designs of nanoantennas have been proposed. For example bow-tie antennas can focus light beyond the diffraction limit[47,48] and optical resonance antennas can give rise to such high local fields in the feed gap that supercontinuum is generated[49]. In addition, self-similar chains have been predicted theoretically to be a viable design for nanofocusing[50,51], as also recently shown experimentally[43]. Nanoshells can also be used as optical antennas. They have well-distinguished multipolar radiation patterns, which can be selected with the wavelength of the excitation[52]. However, the surface roughness can affect the emission patterns[53]. Down-scaled traditional antennas have also been successfully constructed[54] and tuning of gap antennas loaded with plasmonic materials have been proposed[55]. Even specialized antenna designs like the Yagi-Uda antenna geometry have been proposed[56,57].

There is a wealth of technical expertise dedicated to antenna construction in the radio and microwave domains. To take advantage of this know-how, there is an increasing interest for developing optical equivalents to lumped elements (resistances, inductances, etc.) from the circuit theory[58]. One of the major difficulties in merging these two domains is that the materials exhibit a very different behavior in the optical regime, compared to their behavior at lower frequencies. Specifically, as the skin depth of the metals approaches the feature sizes of the metal structures, the simple rule-of-thumb arguments from antenna theories cease to apply as such[27].

Metamaterials

In a broad sense, metamaterials can be described as artificial materials composed of designer nanostructures that possess properties not usually found in nature. All nanoparticle structures fit within this scope. A stricter classification of metamaterials is that they are engineered materials for which the real parts of either the permittivity ϵ or permeability μ (or both) are negative and usually their optical properties can be described using the effective medium theory. The effective medium theory assumes that the structures comprising the particular metamaterial are small compared to wavelength, so using ϵ and μ is valid. In the visible part of the electromagnetic spectrum, this assumption is extremely demanding even for the contemporary nanofabrication technologies and care must be taken when applying it.

One of the characteristic features related to metamaterials is the negative refractive index. As we saw earlier, a necessary prerequisite for plasmons is that the real part of ϵ is negative. Most metals meet this condition over fairly large a frequency range. A sufficient condition for rendering the real part of refractive index negative, is that real parts of both ϵ and μ are negative, although other strategies are also available[59].

Having $\mathrm{Re}\,\mu < 0$ implies the presence of a magnetic resonance. These resonances do not occur naturally in the optical regime, but with clever design, they can be brought there[60–62]. These resonances can also influence SHG efficiency. For example, split-ring resonator structures have been observed to enhance SHG when a magnetic resonance[63,64] was excited. The possibility of having $\mu \neq 1$ in optical frequencies, or optical magnetism, has been dismissed as being nonphysical even by famous textbooks[65]. However, mixed electric and magnetic responses in the optical domain have been successfully utilized to explain optical activity[66] and magnetization leading to nonlinear optical effects[67].

Various other designs for metamaterials have been proposed as well. Wire pairs have been demonstrated to produce negative index of refraction at around 15 GHz[68] and negative index fishnet structures operating at 2 μm[69]. Multilayered structures have been proposed and predicted to operate at a range of 550-665 nm[70].

Metamaterials are expected to open up new possibilities in optical engineering, including cloaking devices to render objects invisible[71,72] and superlenses that can image objects beyond the traditional diffraction limit[73]. Metamaterials composed of chiral nanostructures are also expected to open pathways into studying and possibly even modifying their chiral properties[74,75].

Up to date, most demonstrations of optical and infrared metamaterials have been based on essentially planar structures, although truly three-dimensional structures

are beginning to emerge[76–78].

Nonlinear Optics

SHG is electric-dipole forbidden in structures with a centrosymmetric configuration. Metals with simple cubic lattice structures, such as gold (face-centered cubic[79]), have a center of inversion, and therefore SHG is forbidden in the bulk of these metals. It is important to note, however, that most techniques, in particular the lithographic ones, used to produce metal nanoparticles do not even result in single crystals. Random distribution of the nanocrystals is likely to increase the symmetry even more. The centrosymmetry is nevertheless broken at the interface of two media with different optical functions, however, rendering SHG again dipole-allowed[8].

Local field enhancement is a very interesting and important concept for nonlinear optics. As the nonlinear processes depend on a high power of the field intensity[50,80–83], the concentration of electromagnetic energy into small volumes can enhance these processes by many orders of magnitude. For example, SHG yield from metal particles can be on the order of 10^5 times greater than that from a planar metal surface[22,82,84].

The local-field is also enhanced via the lightning-rod effect when the local radii of curvature of the particles are small, which can also influence SHG yield. SHG from such sharp metal tips have been investigated[85,86]. It has been found that the near-field interaction between the tip and the vicinity of a surface directly modifies the SH signature[85]. It has also been shown that this interaction can be used directly for mapping the local field distribution at the surface[86].

Rough metal surfaces have also been used to enhance second-harmonic generation from different molecules[25,36] in a fashion similar to SERS. These studies have been complemented with near-field studies[87–89] of SHG from such surfaces themselves. These studies demonstrated the localized nature of enhancements due to localized surface plamon resonances and particle morphology. Moreover, a strong polarization dependence was found[87].

Modern fabrication methods have enabled almost arbitrary tailoring of shape, size and mutual ordering of the nanoparticles. For second-order nonlinear optical effects, a necessary prerequisite is the lack of centrosymmetry – both on the level of individual particles and on the level of their arrangement. For simplicity, it is beneficial to work with simple planar structures. The simplest two-dimensional noncentrosymmetric structure is the L-shape, which is the particle shape studied in this thesis. The second-order nonlinear properties of L-shaped structures have been investigated also elsewhere. For instance, experiments on the decay time of plasma oscillations in sil-

ver nanoparticles have been conducted. It has been found that the decay times are much larger than expected based on the bulk metal dielectric function[90].

Another noncentrosymmetric shape is the T-shape. T-shaped nanodimers have been studied in an attempt to link the peculiarities observed in SHG characteristics to the corresponding fundamental frequency local-field distributions[91,92]. It was found that for enhanced SHG, high field concentration alone may not be sufficient. Rather, the symmetry of the field distribution in the nanodimers needs also to be low enough to fully support SHG[91].

Self-similar chains, or chains of spheres whose radii and separations decrease with a constant factor, have been proposed as an efficient way to localize light in an efficient and controlled manner[50]. They have also been predicted to yield strong enhancement of SHG. The applicability of self-similar chains in field enhancement has been recently demonstrated experimentally for SERS[43], but experimental realizations employing self-similar chains to enhance SHG are yet to be published.

The role of unintentional defects in SHG response of metal nanoparticles is one of the key themes in this work. They are found to greatly influence the details of SHG process (to be discussed in detail in Chapter 6). The effect of "nanoroughness" has been analyzed on the basis of Green's function theory with the result that the resulting local SH fields are localized into "hot spots" and strongly incoherent[82]. Near-field mappings[89] demonstrate that the local SHG indeed follows this kind of behavior.

Defects can also act as symmetry-breaking agents, which is also a key topic in this thesis. Symmetry-forbidden SHG signals have been observed from individual nanodots of high symmetry[93], from which also THG was observed. Furthermore, THG was detected for symmetry-forbidden polarization combinations. The details of both SHG and THG were found to vary from particle to particle, which implies that the defects are distributed inhomogeneously among the particles and they dominate the nonlinear responses.

Also other nonlinear processes can benefit from field enhancements in metal structures. For instance, third-harmonic generation has been observed[64,93–95] from metal structures and gratings. THG has been found to be enhanced by many orders of magnitude when a surface plasmon resonance is excited. The nature of this resonance may depend on the exact configuration and morphology of the system. Four-wave mixing has also been investigated from coupled nanoparticles[96]. As the interparticle separation approached contact point, the mixing process grew in intensity by four orders of magnitude, only to change abruptly at contact, when a dimer was formed. Four-wave mixing has also been employed to excite nonlinear surface plasmons[97] in a gold film. It was found that the excitation of the surface plasmons via four-wave

mixing was dominated by the third-order surface susceptibility, rather than bulk susceptibility.

Nanoapertures

Due to the lossy nature of metals, one could expect that a metal film perforated with sub-wavelength holes should transmit very little light. However, this is not the case. In fact, much more light can be transmitted through such "nanohole arrays" than could be expected on the basis of the open area of the nanoholes[98]. This extraordinary transmission is attributed to plasmonic interactions in the walls of the holes. These plasmons are seen to exhibit a hybrid character, combining localized plasma oscillations and long-range propagating plasmons[99].

Nanoapertures can also enhance second-harmonic generation through plasmonic interactions. A bull's-eye pattern of concentric grooves centered around a nanohole has been studied[100] and it has been found to enhance SHG efficiency by a factor of 120. As SHG is a very symmetry-sensitive process, breaking the array symmetry by arranging the nanoholes in a random fashion has been found to favor SHG, compared to a regular array[101]. Locally less-symmetric double-hole arrays have also been observed to enhance SHG, when the separation of the double holes is such that sharp tips are formed in the nanohole[102].

Holes can also be formed in the shape of split-ring resonators (SRR). The discussion on metamaterials consisting of SRRs is complemented by second-harmonic experiments on a SRR-perforated metal film[103]. The differences between Refs. [63,103] were discussed in terms of the Babinet's principle and it was found that for the complementary structures, the roles of the magnetic and electric interactions must be interchanged.

Multipole Effects

The role of multipole effects in SHG response of metal nanoparticles turned out to be one of the main results of this Thesis. It is important to note that one should distinguish between two different types of multipoles when discussing the optical responses of nanostructured materials. The first type arises from the light-matter interaction Hamiltonian and corresponds to microscopic multipole moments on the atomic or molecular level. Such multipoles can enable second-order nonlinear effects from centrosymmetric materials[104], which are forbidden within the electric-dipole approximation of the light-matter interaction.

The second type of multipoles arises from Mie scattering theory[24]. The standard Mie theory is based on a dipolar microscopic interaction, and effective multipoles arise from size and retardation effects. Usually, the optical responses of particles that are small compared to the wavelength can be described in terms of electric dipoles only[22]. However, when the particle size approaches the wavelength, the dipolar picture may no longer provide a complete description, and higher multipoles should also be considered. Both microscopic and effective multipoles, however, lead to similar radiation patterns in the far field. We will mainly be concerned with the second type of multipoles, although both types are considered in Chapter 4.

Nanoparticles that are a lot smaller than the wavelength, support only dipolar plasma oscillation modes[52,105]. As the particle size increases, new higher-order plasma oscillation modes such as quadrupole modes start to emerge. These modes create new bands in the extinction spectrum of nanoparticles[105]. Usually these higher-order oscillation modes are resonant at a higher energy (shorter wavelengths), but the fine details depend sensitively on the geometry of the particular particle. With careful engineering, the extinction peaks corresponding to different modes can be separated by tens or even hundreds of nanometers[52,105,106].

It is important to note that the size- and shape-dependence of the extinction bands do not necessarily mean that these modes represent different multipolar modes. For example, in the extinction spectrum of a rectangle-shaped nanostructure, there will be at least two dipolar extinction resonances, corresponding to the two orthogonal polarizations of the excitation. These peaks are not necessarily multipolar in character.

The contribution of multipoles to the linear optical responses of metal nanoparticles has been discussed in the literature[21,52,105,107–114]. For example, metallic nanoshells can be driven selectively into dipolar and quadrupolar oscillation patterns[52]. Size-dependence of multipolar plasmon resonances from elongated silver nanoparticles has also been studied[105], and predictions of the multipolar character of charge density distributions in triangular nanoprisms have been published[110]. Multipolar plasmon resonances have been observed with scanning near-field microscope[115,116].

Multipole effects can also play a role in the nonlinear responses of metal nanoparticles, including SERS[117], hyper-Rayleigh scattering[118–121] and SHG[122–126]. Of particular interest is hyper-Rayleigh scattering, which corresponds to incoherent scattering of SHG radiation. Such scattering can arise even from centrosymmetric particles due to retardation effects. On the other hand, dipolar radiation patterns can provide direct evidence of symmetry breaking of individual particles even though the macroscopic sample is centrosymmetric.

4 Theoretical Background

In this chapter we introduce the theoretical framework on which this Thesis is based. We begin by briefly discussing the multipole expansion and some implications of it. The Mie scattering theory is introduced and its relation to multipole expansion is discussed. After that we move on to discuss the multipoles arising from the microscopic light-matter interaction and how they affect the second-harmonic generation process. Finally, we introduce and discuss a simple phenomenological model of multipolar responses arising from surface defects and show how these defects can be used to to account for symmetry-forbidden SHG.

4.1 Potentials as Solution to Maxwell Equations

Although in Section 2 we solved the electrodynamic problem by formulating the wave equation directly for the electric field $\boldsymbol{E}$, it is often easier to obtain solutions to the Maxwell equations,

$$\begin{aligned} \nabla \cdot \boldsymbol{D} &= \rho, & \nabla \times \boldsymbol{E} &= -\frac{\partial \boldsymbol{B}}{\partial t}, \\ \nabla \cdot \boldsymbol{B} &= 0, \quad \text{and} & \nabla \times \boldsymbol{H} &= \boldsymbol{J} + \frac{\partial \boldsymbol{D}}{\partial t}, \end{aligned} \tag{2.1}$$

indirectly by expressing them as potentials. The potentials transform the coupled first-order partial differential equations into a smaller number of second-order partial differential equations. Since $\nabla \cdot \boldsymbol{B} = 0$, the magnetic induction can be defined in terms of the vector potential $\boldsymbol{A}$

$$\boldsymbol{B} = \nabla \times \boldsymbol{A}. \tag{4.1}$$

Therefore, the electric field can expressed as the gradient of a scalar potential Φ and the time derivative of $\boldsymbol{A}$:

$$\boldsymbol{E} = -\nabla\Phi - \frac{\partial \boldsymbol{A}}{\partial t} \tag{4.2}$$

Gauge Transformations

The potential functions $\boldsymbol{A}$ and Φ are not unique descriptions of the fields $\boldsymbol{B}$ and $\boldsymbol{E}$. The fields remain unchanged if we perform simultaneously the transformations

$$\begin{aligned} \boldsymbol{A} &\rightarrow \boldsymbol{A}' = \boldsymbol{A} + \nabla\Lambda \quad \text{and} \\ \Phi &\rightarrow \Phi' = \Phi - \frac{\partial\Lambda}{\partial t}. \end{aligned} \tag{4.3}$$

From these coupled transformations follows the Lorenz condition[9] for the set of potentials $(\boldsymbol{A}, \Phi)$

$$\nabla \cdot \boldsymbol{A} + \frac{1}{c^2}\frac{\partial\Phi}{\partial t} = 0, \tag{4.4}$$

which is satisfied with the relation

$$\nabla^2\Lambda - \frac{1}{c^2}\frac{\partial^2\Lambda}{\partial t^2} = 0, \tag{4.5}$$

provided that potentials $(\boldsymbol{A}, \Phi)$ in Eq. (4.3) satisfy the Lorenz condition (4.4) initially. This restricted set of potentials belong to the *Lorenz gauge*. It is commonly used, as it will lead to uncoupled wave equations for both scalar and vector potentials and it is independent of the chosen coordinate system, allowing thus the inclusion of the finite speed of light into the potentials, i.e., the delayed potentials[9].

4.2 Multipole Expansion

Multipole expansion is a series expansion where a function is expanded in terms of an expansion parameter which becomes small as the "distance" from a source region becomes larger, therefore allowing us to retain, in most cases, only the first leading term ('multipole') of the series. As an example in electrostatics, physically these multipoles correspond to systems of one, two, four etc. charges.

Static fields

We go through the multipole expansion for the scalar and vector potentials in an introduction-like manner. For simplicity, we start with the non-radiating case, so as to demonstrate the links between the multipoles and physical objects.

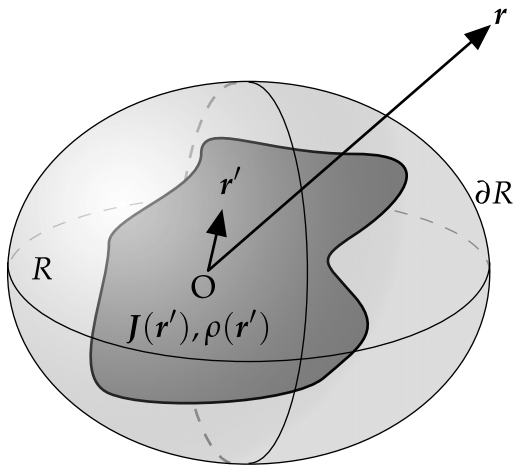

Figure 4.1 Geometry in which the multipole expansion is performed. Primed coordinates refer to points in the source volume and unprimed to those of the observation point. Volume R is chosen to contain the source volume so that the charge and current density $\boldsymbol{J}(\boldsymbol{r}')$ vanish on its surface ∂R.

Electric Fields

Consider a charge distribution (Fig. 4.1), described by the charge density $\rho(\boldsymbol{r}')$. Then construct a volume R which confines the charge distribution so that it vanishes at the boundary ∂R of this volume. The role of R is to divide space into two zones, one containing the charges and the other one being charge-free.

As this problem is time-independent, Eq. (4.2) allows us to express the electric field in terms of the scalar potential Φ only. The scalar potential at $\boldsymbol{r}$ outside R due to the charge distribution is given by[9,127]

$$\Phi(\boldsymbol{r}) = \frac{1}{4\pi\epsilon_0} \int_R \frac{\rho(\boldsymbol{r}')}{|\boldsymbol{r} - \boldsymbol{r}'|} \mathrm{d}V', \tag{4.6}$$

where primed and unprimed coordinates refer to the charge distribution and observation point, respectively.

Using Taylor expansion on $1/|\boldsymbol{r} - \boldsymbol{r}'|$ with respect to $\boldsymbol{r}'$ around the origin $\boldsymbol{r}' = 0$ and

substituting back into in Eq. (4.6) yields

$$\begin{aligned}\Phi(\boldsymbol{r}) &= \frac{1}{4\pi\epsilon_0}\Bigg[\int_R \frac{\rho(\boldsymbol{r}')}{r}\mathrm{d}V' \\ &\quad + \int_R \nabla'\left(\frac{1}{|\boldsymbol{r}-\boldsymbol{r}'|}\right)_{\boldsymbol{r}'=0}\cdot\boldsymbol{r}'\,\rho(\boldsymbol{r}')\mathrm{d}V' \\ &\quad + \int_R \frac{1}{2}\boldsymbol{r}'\cdot H'\left(\frac{1}{|\boldsymbol{r}-\boldsymbol{r}'|}\right)_{\boldsymbol{r}'=0}\cdot\boldsymbol{r}'\,\rho(\boldsymbol{r}')\mathrm{d}V' + \cdots\Bigg], \end{aligned} \tag{4.7}$$

where the operator H' is a dyadic second-order partial derivatives operator*. Keeping with this notation, the differentiation operations may be evaluated to obtain expressions containing the few lowest order multipole moments

$$\begin{aligned}\Phi(\boldsymbol{r}) &= \frac{1}{4\pi\epsilon_0}\left[\int_R \frac{\rho(\boldsymbol{r}')}{r}\mathrm{d}V' + \int_R \frac{\boldsymbol{r}'\rho(\boldsymbol{r}')}{r^3}\mathrm{d}V'\cdot\boldsymbol{r}\right. \\ &\quad \left. + \boldsymbol{r}\cdot\int_R \frac{1}{2}\frac{3\boldsymbol{r}'\boldsymbol{r}' - |\boldsymbol{r}'|^2\mathbf{1}}{r^5}\rho(\boldsymbol{r}')\mathrm{d}V'\cdot\boldsymbol{r} + \cdots\right] \\ &= \frac{1}{4\pi\epsilon_0}\left[\frac{q}{r} + \frac{\boldsymbol{p}\cdot\boldsymbol{r}}{r^3} + \frac{1}{2}\frac{\boldsymbol{r}\cdot\boldsymbol{Q}\cdot\boldsymbol{r}}{r^5} + \cdots\right] \end{aligned} \tag{4.8}$$

where q is the total charge within R, and $\boldsymbol{p}$ and $\boldsymbol{Q}$ are, respectively, dipole and quadrupole moments of the charge distribution. The dipole, quadrupole, etc. moments are related to the charge density through its first, second, etc. moments, which are explicitly expressed as

$$\boldsymbol{p} = \int_R \boldsymbol{r}'\rho(\boldsymbol{r}')\mathrm{d}V' \tag{4.9}$$

$$\boldsymbol{Q} = \int_R (3\boldsymbol{r}'\boldsymbol{r}' - r'^2\mathbf{1})\rho(\boldsymbol{r}')\mathrm{d}V'. \tag{4.10}$$

In Eq. (4.8) and (4.10) the notation $\boldsymbol{r}'\boldsymbol{r}'$ stands for dyadic multiplication, and thus yields a tensor out of its constituent vectors. In the case of quadrupole moment tensor, this product is a symmetric, traceless second-rank tensor, where the symmetry follows directly from the commutation property of scalar multiplications in dyad $\boldsymbol{r}'\boldsymbol{r}'$ and the tracelessness follows from the subtraction of term $r'^2\mathbf{1}$. This is the irreducible representation of the quadrupole moment tensor[9,14].

In the time-independent case, the electric field is directly attainable from the scalar potential Φ by using Eq. (4.2). For electric dipoles the electric field is in the dyadic form:

$$\begin{aligned}\boldsymbol{E}_{\boldsymbol{p}} &= -\nabla\Phi_{\boldsymbol{p}} \\ &= \frac{3\boldsymbol{r}\boldsymbol{r} - r^2}{r^5}\cdot\boldsymbol{p} \end{aligned} \tag{4.11}$$

*More commonly this operator is known as the Hessian matrix.

Magnetic Fields

The multipole expansion of the scalar potential Φ was found to yield the electric quantitities like electric dipoles and electric quadrupoles and so on. To discuss their magnetic counterparts, we first note that the magnetic quantities arise from the current density $\boldsymbol{J}$ rather than charge distribution ρ. These two quantities are linked through the charge continuity equation

$$\nabla \cdot \boldsymbol{J} = \frac{\partial \rho}{\partial t}, \tag{4.12}$$

which can be interpreted as an implication of charge conservation. Therefore we turn the discussion to localized, yet still time-independent current density distribution $\boldsymbol{J}$. In this case a convenient choice of the potential function will be the vector potential $\boldsymbol{A}$, given by[9]

$$\boldsymbol{A}(\boldsymbol{r}) = \frac{\mu_0}{4\pi} \int_R \frac{\boldsymbol{J}(\boldsymbol{r}')}{|\boldsymbol{r} - \boldsymbol{r}'|} \mathrm{d}V', \tag{4.13}$$

from which we can derive the magnetic field using the relation of Eq. (4.1).

Expanding the $1/\boldsymbol{r}'$-dependence of Eq. (4.13) in a fashion similar to Eq. (4.8) and keeping only first two terms, we obtain the approximation

$$\boldsymbol{A}(\boldsymbol{r}) = \frac{\mu_0}{4\pi} \left[\frac{1}{r} \int_R \boldsymbol{J}(\boldsymbol{r}') \mathrm{d}V' + \frac{1}{r^3} \int_R \boldsymbol{J}(\boldsymbol{r}') \boldsymbol{r}' \mathrm{d}V' \cdot \boldsymbol{r} + \cdots \right]. \tag{4.14}$$

The first – monopole – term in square brackets vanishes if we first integrate it by parts[†] and then use the divergence theorem to transform the resulting volume integral into a surface integral, which vanishes due to localization of $\boldsymbol{J}$ inside R. The remaining part vanishes because current density is necessarily divergenceless in the static case. This result can be also seen as the nonexistence of magnetic monopoles.

Writing the tensor $\boldsymbol{J}\boldsymbol{r}'$ in the second integral in Eq. (4.14) as a sum of symmetric and antisymmetric portions[14] we obtain

$$\begin{aligned} \boldsymbol{A}(\boldsymbol{r}) &= \frac{\mu_0}{4\pi} \frac{1}{r^3} \cdot \frac{1}{2} \int_R [\boldsymbol{J}\boldsymbol{r}' + \boldsymbol{r}'\boldsymbol{J}] + [\boldsymbol{J}\boldsymbol{r}' - \boldsymbol{r}'\boldsymbol{J}] \mathrm{d}V' \cdot \boldsymbol{r} \\ &= \frac{\mu_0}{4\pi} \frac{1}{r^3} \cdot \frac{1}{2} \int_R [\boldsymbol{J}\boldsymbol{r}' - \boldsymbol{r}'\boldsymbol{J}] \mathrm{d}V' \cdot \boldsymbol{r} \\ &= \frac{\mu_0}{4\pi} \frac{1}{r^3} \int_R \frac{1}{2} \boldsymbol{r}' \times \boldsymbol{J} \mathrm{d}V' \times \boldsymbol{r} \end{aligned} \tag{4.15}$$

where we have again made use of integration by parts[‡] and the divergence theorem. The current continuity relation [Eq. (4.12)] reduces in the static case to divergenceless

[†] $\nabla \cdot (\boldsymbol{J}\boldsymbol{r}') = (\nabla \cdot \boldsymbol{J})\boldsymbol{r}' + \boldsymbol{J}$
[‡] $\nabla \cdot (\boldsymbol{J}\boldsymbol{r}'\boldsymbol{r}') = (\nabla \cdot \boldsymbol{J})\boldsymbol{r}'\boldsymbol{r}' + \boldsymbol{J}\boldsymbol{r}' + \boldsymbol{r}'\boldsymbol{J}$

of current density.

Moreover, we used the vector triple product[§] to simplify the antisymmetric part, alongside with the dot product representation of tensor contraction[¶]. Defining magnetic dipole moment $\boldsymbol{m}$ as the integrand of Eq. (4.15),

$$\boldsymbol{m} = \frac{1}{2}\int_R \boldsymbol{r}' \times \boldsymbol{J}\mathrm{d}V', \tag{4.16}$$

the vector potential reduces to the form

$$\boldsymbol{A}(\boldsymbol{r}) = \frac{\mu_0}{4\pi}\frac{\boldsymbol{m}\times\boldsymbol{r}}{r^3}. \tag{4.17}$$

To conclude this section, we saw that when we have static charges and currents confined within volume R, we may expand the appropriate potential functions in terms of the electric and magnetic multipole moments. These moments correspond to the first, second, etc. moments of the charge and current distributions. Physically the different moments are related to electrically neutral ensembles of charges and current loops.

Radiating Systems

Now that we have built the basic understanding of the multipole expansion, we move from static systems to time-dependent fields and radiation from localized oscillating sources. We again decompose the arbitrary time-dependence of the oscillation via Fourier expansion into a superposition of time-harmonic oscillation. The linearity of Maxwell's equations (and the resulting partial differential equations) allows each frequency component to be handled separately. Therefore we consider a system of charges and currents as follows:

$$\rho(\boldsymbol{r}', t) = \rho(\boldsymbol{r}')\,\mathrm{e}^{-i\omega t} \quad \text{and} \tag{4.18}$$

$$\boldsymbol{J}(\boldsymbol{r}', t) = \boldsymbol{J}(\boldsymbol{r}')\,\mathrm{e}^{-i\omega t}\,. \tag{4.19}$$

The current continuity equation Eq. (4.12) yields in the case of time-harmonic oscillation

$$\nabla\cdot\boldsymbol{J} = i\omega\rho. \tag{4.20}$$

Using the Maxwell's equations for the curl of magnetic field $\boldsymbol{B}$ and electric field $\boldsymbol{E}$ and the definition of magnetic field though vector potential $\boldsymbol{A}$ [Eq. (4.1)] allows us to

[§] $(\boldsymbol{a}\times\boldsymbol{b})\times\boldsymbol{c} = -(\boldsymbol{b}\cdot\boldsymbol{c})\boldsymbol{a} + (\boldsymbol{a}\cdot\boldsymbol{c})\boldsymbol{b}$
[¶] $\boldsymbol{A}\cdot(\boldsymbol{B}\boldsymbol{C}) = (\boldsymbol{A}\cdot\boldsymbol{B})\boldsymbol{C}$

neglect the scalar potential Φ and focus only on $\boldsymbol{A}$. In the Lorenz gauge, the vector potential is obtained with the help of retarded Green's functions as[9]

$$\boldsymbol{A}(\boldsymbol{r},t) = \frac{\mu_0}{4\pi}\,\mathrm{e}^{-i\omega t}\int_R \frac{\boldsymbol{J}(\boldsymbol{r}')e^{ik|\boldsymbol{r}-\boldsymbol{r}'|}}{|\boldsymbol{r}-\boldsymbol{r}'|}\mathrm{d}V', \tag{4.21}$$

where $k = \omega/c$ is the wave number. Since the magnetic and electric fields are related to vector potential $\boldsymbol{A}$ through the curl operator it is immediately seen that current density $\boldsymbol{J}$ oscillating at frequency ω leads to oscillating magnetic and electric fields at frequency ω.

In some applications, like for example antenna applications, the current density $\boldsymbol{J}$ may be a known quantity and electromagnetic fields may be obtained directly from the integration of Eq. (4.21). Especially in optics, however, this is not the case and we must resort to approximations in order to solve the problem.

First, we note that we are interested in the far-field region, i.e., in the fields sufficiently far from the sources. In this zone, the term $1/|\boldsymbol{r}-\boldsymbol{r}'|$ may be approximated by $1/r$. However, in the exponential of Eq. (4.21) this approximation would be too crude. Therefore, the argument of the exponential is approximated as $|\boldsymbol{r}-\boldsymbol{r}'| \approx r - \hat{\boldsymbol{r}}\cdot\boldsymbol{r}'$. Moreover if the source dimensions are small compared to wavelength, the exponential may be expanded in power series leading to

$$\boldsymbol{A}(\boldsymbol{r},t) = \frac{\mu_0}{4\pi}\frac{\mathrm{e}^{i(kr-\omega t)}}{r}\sum_n \frac{(-ik)^n}{n!}\int_R \boldsymbol{J}(\boldsymbol{r}')(\hat{\boldsymbol{r}}\cdot\boldsymbol{r}')^n\mathrm{d}V'. \tag{4.22}$$

We next consider the first two terms of Eq. (4.22), rewriting the $n=1$ term in dyadic notation

$$n = 0: \qquad \boldsymbol{A}_{\boldsymbol{p}}(\boldsymbol{r},t) = \frac{\mu_0}{4\pi}\frac{\mathrm{e}^{i(kr-\omega t)}}{r}\int_R \boldsymbol{J}(\boldsymbol{r}')\mathrm{d}V' \tag{4.23}$$

$$n = 1: \qquad \boldsymbol{A}_{\boldsymbol{Q},\boldsymbol{m}}(\boldsymbol{r},t) = \frac{\mu_0}{4\pi}\frac{\mathrm{e}^{i(kr-\omega t)}}{r}\int_R [\boldsymbol{J}(\boldsymbol{r}')\boldsymbol{r}']\cdot\hat{\boldsymbol{r}}\mathrm{d}V' \tag{4.24}$$

Eq. (4.23) can be cast into a more familiar form of charge distribution ρ using again integration by parts and then using the divergence theorem with the choice of the volume of integration R extending outside the current density distribution, so that the current density $\boldsymbol{J}$ vanishes on surface ∂R. Finally employing the current continuity

equation we have

$$\begin{aligned} \boldsymbol{A}_{\boldsymbol{p}}(\boldsymbol{r},t) &= -i\omega\frac{\mu_0}{4\pi}\frac{\mathrm{e}^{i(kr-\omega t)}}{r}\int_R \boldsymbol{r}'\rho(\boldsymbol{r}')\mathrm{d}V' \\ &= -i\omega\frac{\mu_0}{4\pi}\frac{\mathrm{e}^{i(kr-\omega t)}}{r}\boldsymbol{p}, \end{aligned} \tag{4.25}$$

where $\boldsymbol{p}$ is the electric dipole moment introduced in Eq. (4.9).

In Eq. (4.24) we split the integrand into two parts, one symmetric and the other antisymmetric with respect to the exchange of $\boldsymbol{J}$ and $\boldsymbol{r}'$ and rewrite the antisymmetric part using the vector triple product identity to obtain

$$\begin{aligned} \boldsymbol{A}_{\boldsymbol{Q},\boldsymbol{m}}(\boldsymbol{r},t) &= \frac{\mu_0}{4\pi}\frac{\mathrm{e}^{i(kr-\omega t)}}{r}\int_R \boldsymbol{J}\boldsymbol{r}'\cdot\hat{\boldsymbol{r}}\mathrm{d}V' \\ &= \frac{\mu_0}{4\pi}\frac{\mathrm{e}^{i(kr-\omega t)}}{r}\frac{1}{2}\int_R[(\boldsymbol{J}\boldsymbol{r}'+\boldsymbol{r}'\boldsymbol{J})]\cdot\hat{\boldsymbol{r}}+[\boldsymbol{r}'\times\boldsymbol{J}]\times\hat{\boldsymbol{r}}\,\mathrm{d}V' \\ &= \boldsymbol{A}_{\boldsymbol{Q}}+\boldsymbol{A}_{\boldsymbol{m}}, \end{aligned} \tag{4.26}$$

The antisymmetric part can be immediately identified as magnetic dipole moment, cf. Eq. (4.16), giving

$$\boldsymbol{A}_{\boldsymbol{m}} = ik\frac{\mu_0}{8\pi}\frac{\mathrm{e}^{i(kr-\omega t)}}{r}\boldsymbol{m}\times\hat{\boldsymbol{r}}. \tag{4.27}$$

Using the same procedure of integration by parts as when deriving the magnetic dipole moment, we arrive to a more familiar form for the vector potential, namely

$$\boldsymbol{A}_{\boldsymbol{Q}} = -\frac{\mu_0 ck^2}{8\pi}\frac{\mathrm{e}^{i(kr-\omega t)}}{r}\int_R \rho(\boldsymbol{r}')\boldsymbol{r}'\boldsymbol{r}'\mathrm{d}V'\cdot\hat{\boldsymbol{r}} = -\frac{\mu_0 ck^2}{8\pi}\frac{\mathrm{e}^{i(kr-\omega t)}}{r}\boldsymbol{Q}\cdot\hat{\boldsymbol{r}}, \tag{4.28}$$

where $\boldsymbol{Q}$ is the quadrupole moment from electrostatics [Eq. (4.10)].

Fields from Multipoles

Having now obtained the vector potentials corresponding to the different multipolar orders, we can extract the respective electric fields from the vector potential through repeated application of the curl operator:

$$\boldsymbol{E} = i\frac{1}{kc^2}\nabla\times(\nabla\times\boldsymbol{A}),$$

For the electric dipole $\boldsymbol{p}$, we obtain from Eq. (4.25) after some lengthy, but straightforward algebra

$$\boldsymbol{E}_{\boldsymbol{p}} = \frac{k^2}{4\pi\epsilon_0}\frac{\mathrm{e}^{i(kr-\omega t)}}{r}\left[(\hat{\boldsymbol{r}}\times\boldsymbol{p})\times\hat{\boldsymbol{r}}\right] \tag{4.29a}$$

$$+\frac{1}{4\pi\epsilon_0}\mathrm{e}^{i(kr-\omega t)}\left(\frac{1}{r^3}-\frac{ik}{r^2}\right)\left[3\hat{\boldsymbol{r}}\hat{\boldsymbol{r}}-\mathbf{1}\right]\cdot\boldsymbol{p} \tag{4.29b}$$

where only part (4.29a) contributes to radiation in the far field. It is immediately seen that the electric field $\boldsymbol{E}_{\boldsymbol{p}}$ follows the part of the dipole $\boldsymbol{p}$ that is transverse with respect to direction of propagation $\boldsymbol{r}$.

For the magnetic dipole $\boldsymbol{m}$ and electric quadrupole $\boldsymbol{Q}$, we obtain through similar procedure the expressions in the far field

$$\boldsymbol{E}_m = \frac{k^2}{8\pi\epsilon_0}\frac{\mathrm{e}^{i(kr-\omega t)}}{r}(\boldsymbol{m}\times\hat{\boldsymbol{r}}) \qquad \text{and} \tag{4.30}$$

$$\boldsymbol{E}_Q = \frac{k^2}{8\pi\epsilon_0}\frac{\mathrm{e}^{i(kr-\omega t)}}{r}\left[(\hat{\boldsymbol{r}}\times(\boldsymbol{Q}\cdot\hat{\boldsymbol{r}})\times\hat{\boldsymbol{r}}\right], \tag{4.31}$$

where in Eq. (4.31) there is also a tensor contraction involved. Note that this expression implies that the quantity $\boldsymbol{Q}\cdot\hat{\boldsymbol{r}}$ can be interpreted as an effective dipole, which depends on the direction of propagation.

4.3 Multipole Expansion and Optics

The multipole expansion has a broad spectrum of possible applications. When discussing multipoles in the context of nanoparticles, it must be noted that the multipolar interaction can appear in two levels, one of which is the multipoles emerging from the Mie scattering theory and the other one is the microscopic light-matter interaction Hamiltonian.

Mie scattering theory is based on the multipole expansion of the electromagnetic fields and expressing the extinction in terms of these multipolar orders. The microscopic interaction is based on phenomenological models describing the dielectric function of the materials. For the Hamiltonian, the multipoles correspond to the microscopic multipole moments of the transitions between atomic or molecular energy levels.

Here, we outline in more detail these relations between the multipole expansion and the light-matter interaction. We begin with a brief discussion of the Mie scattering and how different multipolar orders are related to it. After that we discuss the con-

nection between nonlinear optics and the relation of differerent multipolar orders to the nonlinear optical response.

Mie Theory of Scattering

In his much-cited paper from 1908[23], Gustav Mie formulated the theory of diffraction of electromagnetic waves by a conducting sphere of homogeneous, but otherwise arbitrary composition and diameter, embedded in a homogeneous medium. The Mie theory is derived for a single sphere only, but can be generalized to account for a collection of spheres – provided that the spheres are of the same size and composition. The spheres must also be randomly distributed at distances which are long compared to wavelength, so that their superposition is just the single sphere response multiplied by their number[128].

The Mie theory is based on applying Maxwell's equations with proper boundary conditions in spherical coordinates. The multipole expansion is applied to the electric and magnetic fields separately, thus decomposing the incident field into a sum of two kinds of 'partial waves'. These partial waves are chosen such that for the first kind the electric field is purely transverse with respect to the propagation direction. For the second kind of partial waves the magnetic field is transverse. Armed with this decomposition, the Maxwell's equations separate into a set of ordinary differential equations in spherical coordinates. The derivation of the solutions have been discussed extensively (see, e.g. Refs. [7,9,22,23,128]), and the details will not be reproduced here.

Mie's solution is to solve the Maxwell's equations by dividing the problem into an electromagnetic problem which is treated *ab initio* and a material problem which is solved using a phenomenological dielectric function $\epsilon(\omega, d)$. The particle radius d is to emphasize that the dielectric function will exhibit dependence on the size of the sphere. The wide applicability of the Mie theory is based on being able to absorb the potentially intractable microscopic details into the dielectric function. The theory is also criticized for this phenomenological character as it is said to give no physical insight into the material properties[22].

Kreibig *et al.*[106] in 1987 made the connection between the extinction spectrum predicted by Mie theory and plasmon oscillations of different multipolar orders. They interpreted the extinction bands in the spectra of spherical nanoparticles in terms of dipolar, quadrupolar etc. modes of the total Mie extinction. Each multipolar mode in the Mie theory is contributed by electric and magnetic modes which are identified to physically arise from surface plasmon polaritons and eddy currents, which in turn, consist of absorption and scattering bands[22,106].

The key parameter in the Mie theory is the size parameter $x = kd$, where $k = \omega/c$ is the wavenumber. Multipoles can also be seen to arise from size and retardation effects. Dadap *et al.* discussed theoretically this aspect in relation to second harmonic Rayleigh scattering[129] and second harmonic generation[119] from small centrosymmetric spheres. There is also experimental evidence of multipolar interactions due to size and retardation effects in the nonlinear optical responses of nanoparticles, see e.g. Refs. [120,121,123,130].

Microscopic Hamiltonian

The microscopic interaction of the nonlinear material and the electric field can be described in terms of the light-matter interaction Hamiltonian. To account for the multipolar orders, we expand the Hamiltonian in various multipolar orders to yield[131]

$$H = -\boldsymbol{p}\cdot\boldsymbol{E} - \boldsymbol{m}\cdot\boldsymbol{B} - \boldsymbol{Q} : \nabla\boldsymbol{E} + \ldots, \tag{4.32}$$

where $\boldsymbol{p}$, $\boldsymbol{m}$, $\boldsymbol{Q}$ are the electric dipole, magnetic dipole and electric quadrupole moments discussed in the previous section, but now interpreted as quantum-mechanical operators. As we saw, the magnetic dipole and electric quadrupole moments are of the same order in the multipole expansion. However, they are expected to be significantly weaker compared to the electric-dipole moment. Symmetry reasons may, however, cancel the electric-dipole contribution to the optical response. In this case, the higher-order terms determine to nature of the optical response.

For the case of second-harmonic generation, the interaction Hamiltonian leads to nonlinear polarization at the SH frequency as[67,132]

$$\begin{aligned}\boldsymbol{P}(2\omega) = \quad & \boldsymbol{\chi}^{eee}(2\omega,\omega,\omega) : \boldsymbol{E}(\omega)\boldsymbol{E}(\omega) \\ & + \boldsymbol{\chi}^{eem}(2\omega,\omega,\omega) : \boldsymbol{E}(\omega)\boldsymbol{B}(\omega) \\ & + \boldsymbol{\chi}^{eeQ}(2\omega,\omega,\omega) \vdots \boldsymbol{E}(\omega)\nabla\boldsymbol{E}(\omega),\end{aligned} \tag{4.33}$$

where superscripts e, m, and Q associate the nature of the interaction with electric dipolar, magnetic dipolar and electric quadrupolar, respectively. To be explicit, the component i of polarization $\boldsymbol{P}(2\omega)$ is

$$\begin{aligned}P_i(2\omega) = \quad & \chi^{eee}_{ijk}(2\omega,\omega,\omega)E_j(\omega)E_k(\omega) \\ & + \boldsymbol{\chi}^{eem}_{ijk}(2\omega,\omega,\omega)E_j(\omega)B_k(\omega) \\ & + \boldsymbol{\chi}^{eeQ}_{ijkl}(2\omega,\omega,\omega)E_j(\omega)\nabla_k E_l(\omega).\end{aligned} \tag{4.34}$$

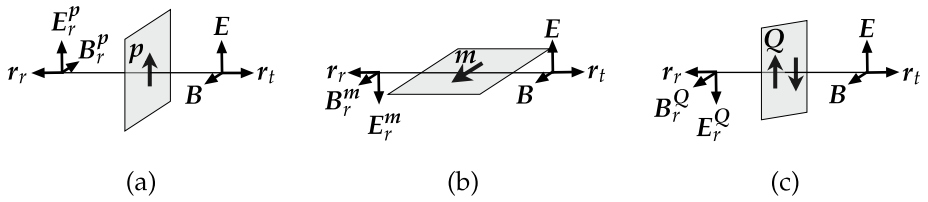

Figure 4.2 Schematic illustration of the differences in radiative properties of electric dipole $\boldsymbol{p}$, magnetic dipole $\boldsymbol{m}$ and electric quadrupole $\boldsymbol{Q}$.

Moreover, the SH response includes also a nonlinear magnetization

$$\boldsymbol{M}(2\omega,\omega,\omega) = \boldsymbol{\chi}^{mee} : \boldsymbol{E}(\omega)\boldsymbol{E}(\omega) \tag{4.35}$$

and quadrupolarization

$$\boldsymbol{Q}(2\omega,\omega,\omega) = \boldsymbol{\chi}^{Qee} : \boldsymbol{E}(\omega)\boldsymbol{E}(\omega). \tag{4.36}$$

These all can act as sources for SH radiation. In materials where the χ^{eee} tensor vanishes due to centrosymmetry, the higher-order multipoles may permit SHG even in the bulk of the material. The reasons for this are that the magnetic quantities are axial, not polar, vectors, whose symmetry properties are therefore different from the electric quantities, and that the quadrupolar interactions lead to tensors of rank four, not three[14,104,133].

4.4 Transformation properties of multipoles

Customarily, different multipolar orders of radiation can be identified by their distinctive radiation patterns in 3-dimensional space. However, in the present work we are concerned with SHG, which is a coherent process and produces strongly directional, laser-like, emission. For the case of surface-like samples, strong emission is obtained only in the transmitted and reflected directions. Therefore, to be able to separate the multipolar orders, we need to understand how the different multipole emissions transform when we reverse the propagation direction of emitted radiation.

Now let's assume that we are observing the electric field at point $\boldsymbol{r}_t$, the transmitted direction (cf. Fig. 4.2). Further, let's assume that the direction of electric field in the transmitted direction, in a given instant in time, is given with vector $\boldsymbol{E}$ for the electric dipole $\boldsymbol{p}$, magnetic dipole $\boldsymbol{m}$ and electric quadrupole $\boldsymbol{Q}$. Then we detect the vectorial amplitude of electric field vectors at point $\boldsymbol{r}_r = -\boldsymbol{r}_t$, called the reflection direction.

Perusing Eq. (4.29a), (4.30), and (4.31) we see that

$$\boldsymbol{E}_p(\boldsymbol{r}_r) = \boldsymbol{E}_p(\boldsymbol{r}_t), \tag{4.37a}$$

$$\boldsymbol{E}_m(\boldsymbol{r}_r) = -\boldsymbol{E}_m(\boldsymbol{r}_t), \quad \text{and} \tag{4.37b}$$

$$\boldsymbol{E}_Q(\boldsymbol{r}_r) = -\boldsymbol{E}_Q(\boldsymbol{r}_t). \tag{4.37c}$$

These differences in the radiative properties of the various multipoles in the transmitted and reflected directions lead to opposite interference effects in the two directions, which provides a basis towards separating the electric dipoles from the magnetic dipoles and electric quadrupoles emitted by some object of study. The magnetic dipoles and electric quadrupoles cannot be distinguished this way, though.

4.5 Nonlinear Response Tensor

In this section, we develop a scattering matrix-like formalism to describe the second-order nonlinear optical responses of our samples Paper 4. First, we note that in nanostructures, the electromagnetic fields, material properties and nonlinear sources can vary over the scale of a wavelength or less[82,83]. To obtain the macroscopic response, the nonlinear responses must be integrated over the entire active structure. The traditional susceptibility formalism outlined in Chapter 2 on the other hand, describes the connection between the driving fields and the nonlinear source polarization by assuming that the material is homogeneous on a scale larger than molecules (or atoms) but smaller than wavelength and then averaging the molecular responses over such scale. The nanoscopic local electric fields are then assumed to be directly proportional to the macroscopic fields, differing only by a material-dependent local-field factor[11]. Moreover, in the standard susceptibility formalism, the different multipolar orders of the light-matter interaction are described by different susceptibilities[16].

Predicting the nonlinear responses via direct integration of the local nonlinear sources can be done phenomenologically for structures of high symmetry, but for structures of more realistic geometries, it is currently exceptionally difficult. Moreover, due to nanoscale gradients, higher multipoles may also contribute to the macroscopic second-order response. To avoid the presently intractable task of integrating at the nanoscale, we have introduced a macroscopic nonlinear response tensor (NRT) formalism, which operates on the level of input and output fields Paper 4. For SHG, the NRT tensor links together a specific polarization component of the SH field to components of the fundamental field in a manner not unlike the SH source polarization

in the susceptibility formalism[11]:

$$E_i(2\omega) = \sum_{jk} A_{ijk} E_j(\omega) E_k(\omega). \tag{4.38}$$

However, important conceptual differences are that the measurable signal field, not the nonlinear source, appears on the left-hand side of Eq. (4.38), and as the NRT formalism describes the relation of vector amplitudes in a given experimental geometry, it implicitly includes the contributions of all nonlinear sources. The NRT is therefore a convenient way to describe the measurable optical responses without worrying about the complicated nanoscale effects. Although the NRT is specific to a given experimental geometry rather than the sample itself, NRTs determined under different experimental conditions can be compared to obtain valuable understanding of the underlying physical processes Paper 5.

4.6 Phenomenological Model of Effective Quadrupoles

In the following, we present a simple phenomenological model that shows how spatially separated elementary dipole sources can give rise to both dipolar and effective quadrupolar sources of radiation. To illustrate the basic idea of the model, we first consider a system of two dipoles with their dipole moments pointing in opposite directions along the y-axis, i.e., $\boldsymbol{p}_1 = -\boldsymbol{p}$ and $\boldsymbol{p}_2 = \boldsymbol{p}$, where $\boldsymbol{p} = p\boldsymbol{y}$. In addition, we assume that that the dipoles are separated by a small vector $\boldsymbol{a} = a_x\boldsymbol{x} + a_y\boldsymbol{y} + a_z\boldsymbol{z}$, and consider emission in the direction $\boldsymbol{k} = k\boldsymbol{z}$ parallel to the z-axis (cf. Fig. 4.3). Such a system cannot give rise to dipolar emission to the far field. Instead, the system acts as an effective quadrupole source, which can be expressed a symmetric sum of a dyad formed from the dipole moment $\boldsymbol{p}$ and the separation vector $\boldsymbol{a}$.

$$\boldsymbol{Q} \propto \boldsymbol{ap} + \boldsymbol{pa}. \tag{4.39}$$

To demonstrate the origin of this result, consider a system of four charges $q_1 = -q$, $q_2 = q$, $q_3 = -q$, and $q_4 = q$. These charges are located at $\boldsymbol{r}'_{1,2} = [-a_x/2, -a_y/2 \pm b/2, -a_z/2]$ and $\boldsymbol{r}'_{3,4} = [a_x/2, a_y/2 \pm b/2, a_z/2]$, see Fig. 4.3.

Taking Eq. (4.10) as our starting point and transforming the integral into sum over charges to produce the quadrupole moment tensor corresponding to the present geometry yields

$$\boldsymbol{Q} = \sum_k q(\boldsymbol{r}'_k)\boldsymbol{r}'_k\boldsymbol{r}'_k. \tag{4.40}$$

Note, however, that for simplicity is quadrupole moment tensor is not in its irreducible state.

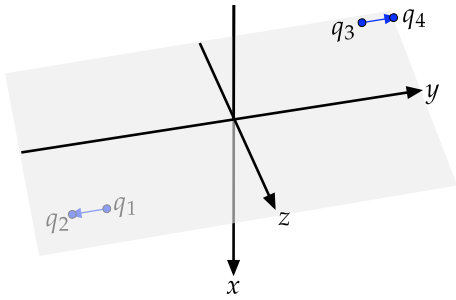

Figure 4.3 Geometry of quadrupole formed from four charges.

The quadrupole moment tensor can be presented as a 3×3 matrix as

$$\boldsymbol{Q} = \begin{pmatrix} 0 & a_x bq & 0 \\ a_x bq & 2a_y bq & a_z bq \\ 0 & a_z bq & 0 \end{pmatrix}. \tag{4.41}$$

where the term bq can be seen as the magnitude of dipole moments formed by the pairs $q_1 + q_2$ and $q_3 + q_4$, or p. Therefore, the quadrupole moment tensor $\boldsymbol{Q}$ is equivalent to the dyadic product in Eq. (4.39).

The polarization of the electric field emitted by this system is given through Eq. (4.31). Considering the state of polarization in the transmitted direction, given by vector $\boldsymbol{k} = k\boldsymbol{z}$, yields y-polarized emission proportional to

$$\boldsymbol{E}_{EQ} \propto iQ_{yz}k\boldsymbol{y} = ia_z pk\boldsymbol{y}. \tag{4.42}$$

This result is seen to depend on the retardation of the two dipolar sources along the direction of emission, i.e., on a_z. Note that the directions of emission $\boldsymbol{k} = k\boldsymbol{z}$ have opposite signs for emission in the forward and backward directions. As a consequence, the emitted wavelets will have opposite phases in the two directions.

Quadrupoles Arising from Defects

We now consider a situation relevant to this work, where the laterally opposite sides of the L-shaped structure have non-equivalent defects as illustrated in Fig. 4.4. These defects are assumed to act as localized dipolar sources of SH radiation. Because the defects are non-equivalent, their dipole moments $\boldsymbol{p}_1$ and $\boldsymbol{p}_2$ can be unequal. In addition, the sources can be localized at different positions on the particles. To be specific, we take the sources to be localized at the surface of the structure otherwise arbitrarily, but at $z = \pm a_z/2$. The total far field emitted in the z-direction by such dipolar

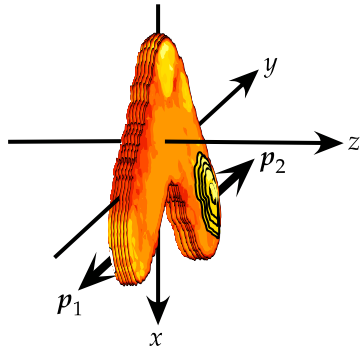

Figure 4.4 Visualization of L-shaped particle where laterally opposite sides have non-equivalent defects.

sources is then proportional to

$$\boldsymbol{E} = \boldsymbol{p}_1 \exp(-ika_z/2) + \boldsymbol{p}_2 \exp(ika_z/2), \tag{4.43}$$

which fully accounts for the phases of the wavelets emitted by both defects. In the spirit of the multipole approach, we expand the exponential to lowest order with respect to the small separation to obtain

$$\boldsymbol{E} = \boldsymbol{p}_1 + \boldsymbol{p}_2 + (\boldsymbol{p}_2 - \boldsymbol{p}_1)ika_z/2, \tag{4.44}$$

whose second term clearly behaves as emission from an effective quadrupole where the two dipoles are mutually retarded, along the lines of Eq. (4.42).

The spatial directions of the dipole sources arising from the surface defects are not limited in any way in this model and they may depend on many different factors, like for example, the excitation, the detailed surface structure and many others. Therefore the actual polarization of the emission from this effective quadrupole source may vary which can be used to our advantage in order to distinguish the contributions of the various types of sources.

5 Experimental Details

```
Some tools are used
     because it's a company policy,
some
     because they are useful.
```

The samples studied in this Work are two-dimensional L-shaped metal nanoparticles, arranged in regular arrays. The metal we chose to use is gold because it is exceptionally well-suited for the excitation of particle plasmons. Another advantage is that gold is chemically stable as it does not, e.g., oxidize when subject to normal laboratory environment.

The shape "L" was chosen because it is the simplest two-dimensional noncentrosymmetric structure, when the two arms of the L are made equal in length. This lack of symmetry is a necessary precondition for the second-order nonlinear optical processes to occur, at least in the electric-dipole approximation[11] and at normal incidence.

5.1 Sample Fabrication

These samples were fabricated at the University of Joensuu by our collaborators. The preparation method was electron-beam lithography (EBL) followed with a standard lift-off process[134]. The process is outlined schematically in Fig. 5.1.

EBL is a versatile fabrication method. Its primary advantage is that it allows patterning of structures beyond the diffraction limit of the feature size imposed by the conventional optical lithography tools employed by the electronics industry. The feature sizes available with current EBL technology are on the order of tens of nanometers, whereas with the equipment available to us for the present work, the feature sizes were on the order of a hundred nanometers.

A key limitation to electron beam lithography is its slow throughput as it can take several hours just to expose a single 1×1 mm sample area. Moreover, the equipment can be particularly sensitive to precise calibration, which is harmful for the repeatibility of the samples.

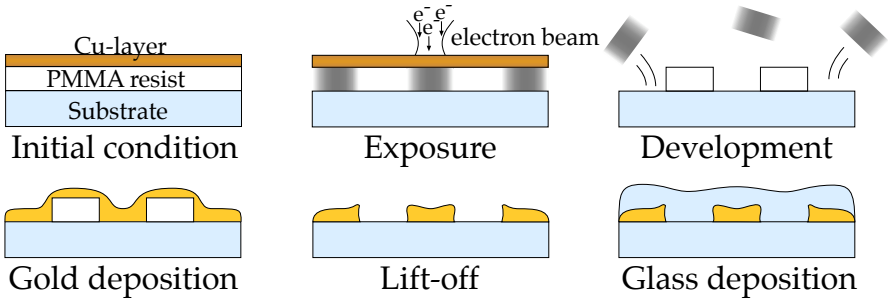

Figure 5.1 Schematic illustration of the process steps in the sample fabrication process.

In the process, a submicron layer of poly(methyl methacrylate) (PMMA) resist was spin-coated on a fused silica substrate. After spin-coating, a 20 nm copper layer was evaporated on top of the PMMA to prevent the sample from becoming electrically charged during the electron-beam exposure.

Nanoparticles were written in the resist by exposing the spin-coated substrate with a controlled electron beam. The copper layer was removed after the exposure, and the resist was developed, removing the exposed regions. The substrate was then covered with a thin layer of chromium followed by a 20 nm layer of gold. The role of the chromium layer between the substrate and the gold was to improve the adhesion of the gold to the substrate. Next, the remaining resist was lifted off, leaving only patterned gold structures. Finally, the sample was covered with a 20 nm protective layer of fused silica. Several sample areas were prepared on the same substrate to allow simultaneous and identical processing and a meaningful comparison between the samples. This is important as the fabrication parameters exhibit variation between different sample batches.

The variations in the fabrication process parameters resulted in a richness of artifacts in the structures. Some of these artifacts are demonstrated in Fig. 5.2, which shows a scanning electron micrograph of one of our samples. The designed sharp corners came out rounded and there are fluctuations in the height profile of the particles. Moreover, the slight astigmatism of the writing electron beam results in structures which have lateral asymmetry. Nevertheless, the structures were still fairly close to their original design. We note however, that some of the samples have significantly better quality than the ones shown in Fig. 5.2.

5.2 Sample Parameters

To gain understanding on the physical origin and nature of the linear and nonlinear responses of the structures, we varied many different parameters of the structures.

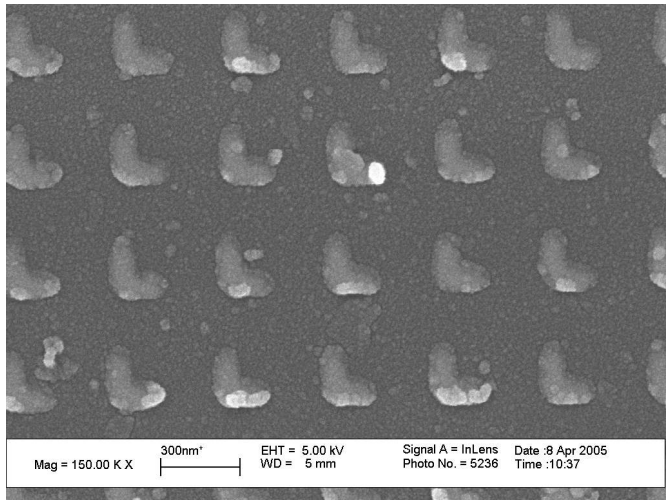

Figure 5.2 Scanning electron micrograph of our samples. The image is presented to show the rich variations in the detailed structure of the nanoparticles. Image taken by Konstantins Jefimovs.

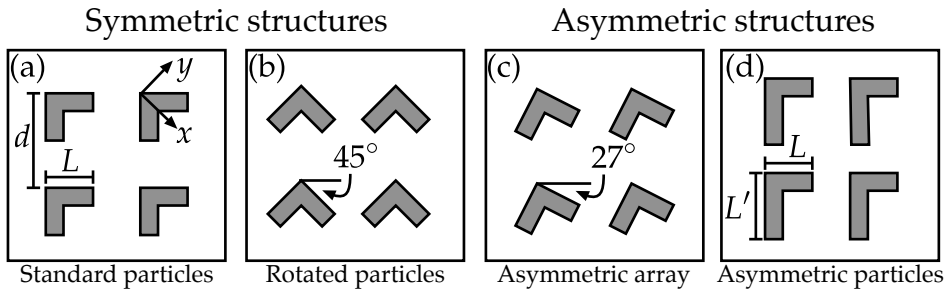

Figure 5.3 Different sample geometries and the associated coordinate system of the samples studied in this work.

The variations in the sample parameters are illustrated in Fig. 5.3.

First, we studied the effect of the particle size by varying the arm length L of the nanoparticles. After that we investigated the possibility of inter-particle effects by changing the period d of the array. The effect of structural symmetry was studied by rotating the particles in their respective unit cells, first by 45° which results in a symmetric structure and does not change its symmetry group. Then a sample was fabricated so that the particles were rotated 27° in their unit cells, which breaks the symmetry of the structure while the particles themselves remain symmetric. Last, the symmetry was broken by designing a structure where the particles are placed in a symmetric array, but particles themselves were asymmetric because they had no longer symmetric arms; $L' > L$.

Coordinate System

The symmetry of the ideal L-shape defines the set of in-plane coordinate axes, where the x-axis bisects the arms of the L (c.f. Fig. 5.3). Ideally the structures would belong to symmetry group C_{1h}, in which the only allowed symmetry operation is a reflection through the symmetry axis – the xz-plane.

5.3 Linear Experiments

Our host of experiments to characterize the samples was begun by a simple but important set of experiments; the characterization of samples' linear optical properties. These properties are important as the nonlinear properties are directly influenced by the linear properties.

Although the linear optical properties are important, they are somewhat insensitive to the finest details of the structures, as we shall show in Chapter 6.

Extinction

We measured the optical density of the samples with a tungsten halogen light source covering the spectral range from 350 nm to 1650 nm and two portable spectrometers, one of which covers the visible spectrum from 350 nm to 1100 nm and the other one that covers the near-infrared region from 900 nm to 1650 nm. Both devices are fiber-coupled for convenient alignment and powerful light collection. The overlap of the spectral ranges provides a nice way to calibrate their responses to produce spectral data for the whole combined spectral range of 350 nm to 1650 nm.

The experimental setup (Fig. 5.4) for the spectral measurements consists of an output fiber for the light source, followed by a collimating lens and a focusing lens. A polarizer is mounted in a rotation stage so that we can freely choose the azimuthal direction of the linear polarization. The polarized light is then focused through a pinhole on the sample. The transmitted light is collected with a pickup fiber, connected to the spectrometer and analyzed with a computer.

For the extinction measurements, we first obtain a reference spectrum by determining the spectrum of the light through the substrate on a spot with no nanoparticles. Having obtained the reference spectrum we measure the spectrum transmitted through the sample. To determine the extinction spectrum from the measurements, we express the extinction spectrum as the ratio of the transmitted and reference spectra.

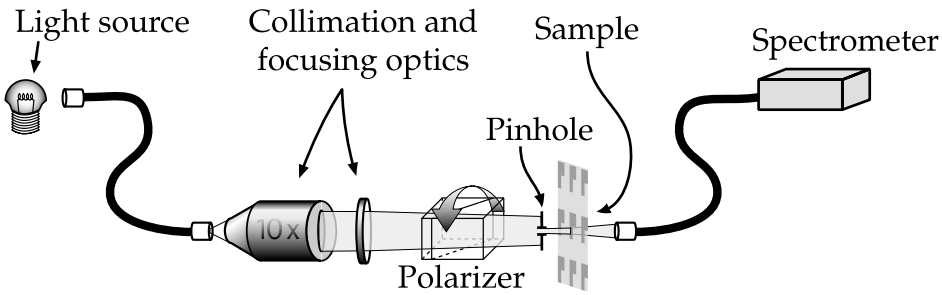

Figure 5.4 Experimental setup for determining the dichroic extinction spectrum.

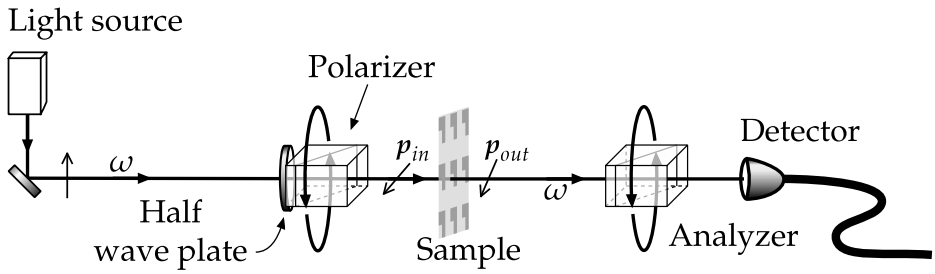

Figure 5.5 Experimental setup for polarization azimuth rotation. The azimuth direction of the incident linear polarization is selected using the combination of half-wave plate and calcite polarizer. The analyzer is used to determine the change in the direction of the polarization.

This unitless quantity is known as the transmissivity (T) and defined by

$$T(\lambda) = \frac{\text{sample}(\lambda)}{\text{reference}(\lambda)}. \tag{5.1}$$

Polarization Azimuth Rotation (PAR)

During our first experiments, we found that our samples change the state of polarization of light transmitted through the sample as described in Papers 1, 2 and Ref. [135]. These experiments were carried out using fixed wavelengths, for which we have a laser light source. We used an experimental setup (Fig. 5.5) where the azimuth direction of linear polarization was chosen with a combination of a half-wave plate and a high-quality calcite polarizer. The purpose of the polarizer was to make sure that the polarization incident on the sample is truly as linear as possible. The state of polarization for the transmitted light was determined with an analyzer and a photodiode.

5.4 Nonlinear Experiments

To characterize the second-order nonlinear optical responses of our samples, we performed different variations of frequency-doubling experiments. In all experiments, the excitation source was a femtosecond laser (Time-Bandwidth Products GLX-200; 200 fs pulse duration, 1060 nm wavelength; 350 mW average power; and 82 MHz pulse repetition rate). The output beam from the laser is linearly polarized with an extinction ratio of roughly 1:200, which allows us to realize power control of the laser beam power by a combination of a half-wave plate followed by a calcite polarizer. The half-wave plate rotates the polarization of the laser beam and the polarizer permits only that fraction of light to pass, which is polarized along the polarizer's pass direction. This arrangement allows us to both a) vary the power of the beam in a continuous manner; and b) make sure that the beam downstream is well-polarized.

The well-polarized laser beam propagated through a beam chopper, chopping it at approximately 1 kHz rate. The second-harmonic emission was detected with a sensitive photo-multiplier tube and a lock-in amplifier referencing the chopper frequency.

The SH emission upstream from the sample was eliminated in the experimental setup with a low-pass, or visible blocking filter to make sure that we only measure SH signals originating from the sample*. After the sample, the infra-red light was blocked by a high-pass, or infrared-blocking filters. Finally, the last element before the detector was a narrow-band interference filter to block any significant two-photon fluorescence from entering the detector. This setup provides the basis for the actual experimental setups.

The experimental results presented in this work are always expressed in relative units, normalized either to unity or with respect to another sample. The reason for not going through the error-prone and cumbersome procedure of calibrating the responses to an absolute scale is that these are the first experiments on these particular types of structures. The goal is to gain basic understanding of the physical phenomena and for that purpose, the responses do not need absolute calibration at this stage. However, the absolute calibration is an important procedure to perform – once we have built the elementary understanding of what really happens in the nanoscale – and must not be forgotten.

The SH signals are weak in magnitude and require sensitive detection apparatus. In order to generate enough SH intensity so that the signal-to-noise ratio is at a comfortable level, the excitation power had to be kept at a fairly high level. With high laser power and metal samples which absorb light, there is always the risk of damaging

*Most polarization optics are made of crystalline materials, usually quartz or calcite, properties of which include excellent SHG yield, at least compared to our samples.

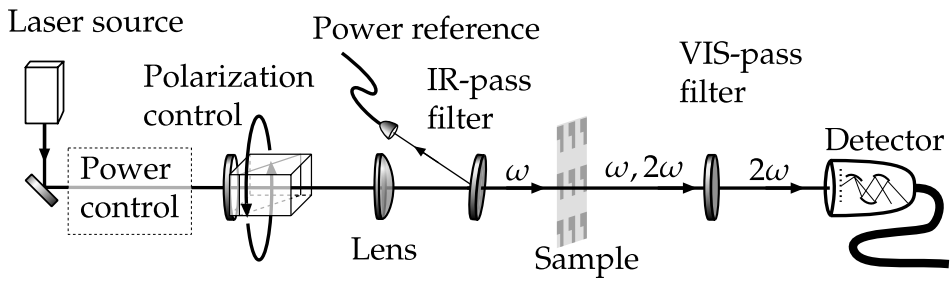

Figure 5.6 Experimental setup for power-law experiments. The azimuth direction of the incident linear polarization is selected using the combination of half-wave plate and calcite polarizer. IR-pass filter blocks the unwanted SH generated in elements upstream from source, whereas the VIS-pass filter blocks the fundamental wavelength from reaching the detector. Detector assembly contains a narrow-band interference filter to block any two-photon fluorescense. The power reference assembly consists of a diffusor plate and a photodiode.

the samples. Therefore the laser power cannot be scaled up arbitrarily with the hope of producing better SHG. That's why a laser source with high peak power and low energy content was needed. A femtosecond laser meets these requirements perfectly.

Power-law verification

Intensity of second-order nonlinear processes is expected to scale as the square of the intensity of applied excitation. In order to verify that the detected SH signals exhibit true square-dependence of the excitation, simple measurements of input power vs. output power were performed. The results of these measurements were reported in Papers 1 and 2.

The experimental setup consisted of the basic setup, plus a pair of a half-wave plate and a cleanup polarizer, both mounted in rotation stage so that we may choose the azimuth direction of the excitation. The setup is illustrated in Fig. 5.6.

As the purpose of these experiments was to determine the input/output power relation, we needed to measure the input power also. A suitable reference signal proportional to the excitation or fundamental intensity was conveniently available from the setup by slightly tilting one of the optical elements upstream from the sample and detecting the weak reflection from this tilted element.

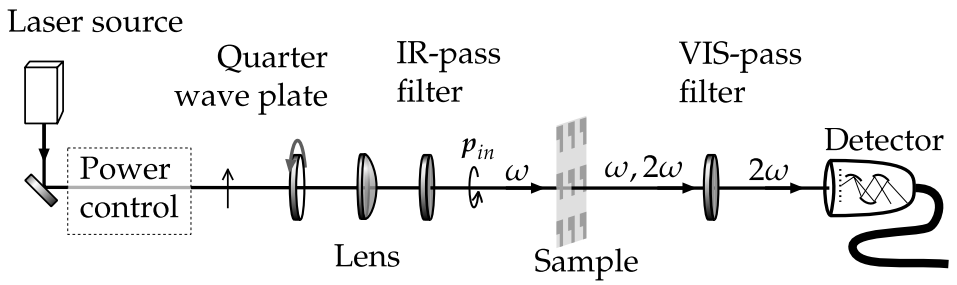

Figure 5.7 Experimental setup for circular difference experiments. The state of polarization of the fundamental beam is varied with the quarter-wave plate in a continuous manner. For circular difference experiments at the fundamental wavelength, the VIS-pass filter is removed and the photomultiplier detector is replaced with a photodiode.

Circular Difference

The second step after the simple power-law experiments was to study the dependence of SHG on the polarization of the fundamental beam. For this purpose, a quarter-wave plate was installed after the clean-up polarizer, so that the state of polarization could be changed in a continuous manner, thus probing the sample with a large number of different elliptical polarization states. The experimental setup is depicted in Fig. 5.7.

Most interesting data points were the ones which corresponded to the left- and right-hand circular states of polarization as these are direct implications of chirality of the samples. These measurements were reported in Paper 3.

Tensorial Dependence

The series of experiments was concluded by experiments designed to address the tensorial nature of SHG. Papers 1, 5, and 6 discuss these experiments and their results. The experiments were performed in two complementary ways. In the first method, part of the second-harmonic response tensor was probed by a combination of linearly polarized fundamental beam and detection of linearly polarized SHG. This method permits only the determination of magnitudes but not phases of "direct" tensor components, e.g. A_{xxx} or A_{xyy} but not a "mixed" component like A_{xxy}.

This method was realized by using the setup from experiments of power-law experiments (Fig. 5.6), with an analyzer added after the sample to pick the desired polarization component of SH light. The second, more involved and detailed method was to use the setup from circular difference experiments as the starting point, and then add an analyzer for SH light after the sample (Fig 5.8). In order to relate both the

relative phases and magnitudes of x- and y-polarized SH sources (components A_{xjk} and A_{yjk}), we need to detect mixed x- and y-polarized signals in addition to detecting pure x- and y-polarized SH light so that components interfere with each other. The laboriousness in this setup comes mostly from this need. In order to access the multipolar contributions in the obtained tensor components, the tensor-dependence data must also be taken in the reflection geometry, as shown in Fig. 5.9.

The obtained data is then fitted to a model function (for details, see Paper 6), which assembles the fundamental electric field components E_x and E_y (in the sample frame) from the azimuthal angles of the waveplates by applying appropriate coordinate transformations to the Jones matrices[128] of the waveplates.

The resulting analytical expression is intimidating at first, but with a clever choice of helper variables it simplifies to the form

$$\boldsymbol{E}_{\text{out}} = -\frac{1}{2}\begin{pmatrix} (i-1)\cos(\alpha) - (1+i)\cos(\beta) \\ (i-1)\sin(\alpha) + (1+i)\sin(\beta) \end{pmatrix} \boldsymbol{E}_{\text{in}}, \tag{5.2}$$

where $\alpha = 2\theta - \delta - \gamma$, $\beta = \gamma - \delta$ and i is the imaginary number, defined by $i = \sqrt{-1}$. Angles δ and θ are the azimuth angles of the fast axes of half and quarter-wave plates in the setup, respectively and angle γ represents orientation of the sample x-axis and it also represents the detected polarization state of SHG. All angles are referenced to the plane defined by the optical table in the laboratory frame.

The electric field components are combined in quadratic combinations, weighted with 12 complex coefficients. These complex coefficients are identified as the tensor components of that nonlinear response tensor which describes the experimental geometry [Paper 6]. They are determined by combining the x-, y-, and $x + y$-polarized SH datasets from a given measurement and fitting them simultaneously to the model

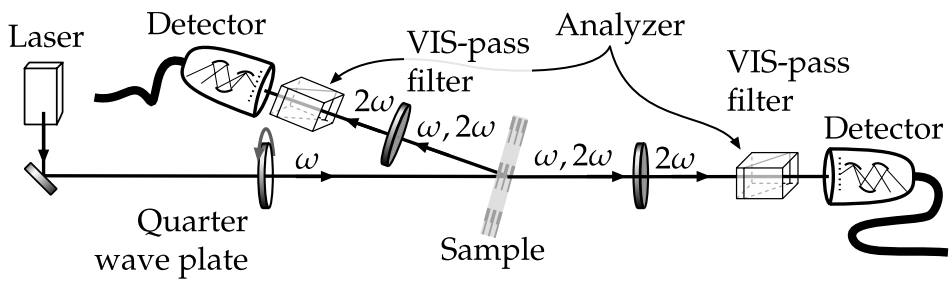

Figure 5.8 Experimental setup for tensor-dependence experiments. The state of polarization of the fundamental beam is varied with the quarter-wave plate in a continuous manner. The second-harmonic light is first polarized with an s-directed analyzer and then detected with photomultipliers. Sample is rotated about its normal to select the determined SH polarization.

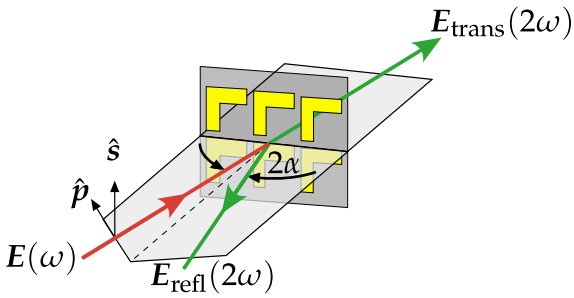

Figure 5.9 Experimental geometry for tensor-dependence experiments.

function. Simultaneous fitting is advantageous as it decreases both the dependence of the fit result on initial values and the relative importance of any one individual dataset[136].

6 Results and Discussion

In this chapter we briefly present and discuss our experimental results. The order in which the experiments are presented is slightly different from the chronological order in which they were published in the Papers.

6.1 Tuning Resonances

Before we discuss the more detailed aspects of the nonlinear responses of our particles, we describe the simpler linear experiments in which we found ways to tune the responses of our samples.

Size

First, we studied the effect of the arm length L on the linear and nonlinear optical properties of the nanoparticles (Fig. 6.1 and 6.2). It can be seen that the particle arrays have very distinctive spectral properties, which directly influence the SH efficiency.

In the spectral range accessible with our instruments these nanostructures have typically three main resonances. The two long-wavelength resonances are strongly polarization-dependent and they were found to red shift towards longer wavelengths with

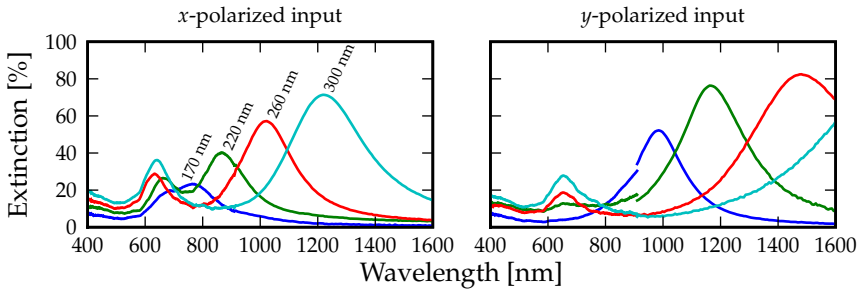

Figure 6.1 Extinction plots for particles where the arm length is varied. Arm lengths: dark blue curves – 170 nm, green curves – 220 nm, red curves – 260 nm, and light blue curves – 300 nm. The two discontinuities in y-polarized input are due to slight discrepancies in transmission calibration. Data partially from Paper 2. Symmetric sample with nanoparticles arranged in normal orientation (cf. Fig 5.3a).

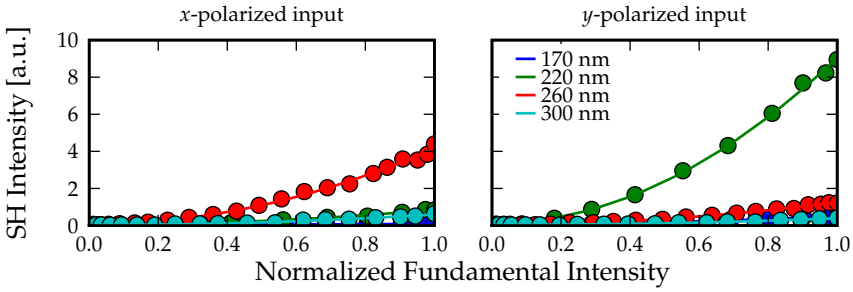

Figure 6.2 SHG curves for particles where the arm length is varied. Arm lengths: dark blue – 170 nm, green – 220 nm, red – 260 nm, and light blue – 300 nm. Solid lines are quadratic fits to SH data. Data published in Paper 2. Symmetric sample with nanoparticles arranged in normal orientation (cf. Fig 5.3a).

increasing L. This was quite expected and typical for particle plasmon resonance behavior. The short-wavelength resonance in the vicinity of ~ 700 nm was found to have only weak polarization dependence. We believe that this extinction resonance is related to the lateral linewidth of the nanostructures, which is nominally kept at constant 100 nm for all of the studied structures.

Fig. 6.2 shows the results of the corresponding SHG power-law measurements, which directly demonstrate that the closer the extinction resonance is to the excitation wavelength, 1060 nm, the better is SHG efficiency. Moreover, stronger resonance (higher extinction) leads to greater efficiency. Therefore, we conclude that for these particular structures, the optimal arm length to be used with our laser is about 200 nm, where the y-polarization is resonant with our laser – for these structures.

Array

Having found the optimal arm length, we investigated the effect of inter-particle coupling through the array structure. The particle size was kept constant, and structures were fabricated so that the inter-particle distance was varied. Also the relative orientation of the particles was varied (cf. Fig 5.3) from the standard orientation to such that particles are rotated 45° (published in Paper 2) and 27° (published in Paper 3) in their respective unit cells.

Overall, the linear and nonlinear responses drop with increasing grating period. This is due to the rather trivial fact that there are fewer particles per unit area to interact with the incident light. It is therefore more meaningful to compare results per particle.

If the electromagnetic wavelets emitted by the particles do not couple together

through the grating structure, possibly modifying the field configuration, the results should remain the same provided that we adjust them for the number of particles per unit area, as the size of individual particles is kept constant. The relevant adjustment for the linear responses is ρ, defined by

$$\rho = \frac{\text{particles}}{\text{unit area}}, \tag{6.1}$$

whereas for SH intensity, the adjustment factor is ρ^2, as SHG is a coherent process where the signal amplitude is the additive quantity.

In Paper 2 we found that the adjusted extinction responses exhibit changes on the order of 30 nm with increasing particle separation. For particles in the 45° rotated orientation, the shift in consistently towards longer wavelength, whereas for particles in standard configuration, the shifts are more inconsistent, but still remain within 30 nm.

In Paper 3 we studied samples from a new batch. This batch included samples with standard orientation and asymmetric samples in which the particles were rotated by 27°. Comparison of the extinction spectra revealed even more pronounced spectral shifts, 50 nm or more. We wish to stress that due to minute changes in the parameters of the fabrication process, a meaningful comparison between samples from different batches is not possible.

Nevertheless, there is one very interesting difference between the very first samples and the following ones. For the first few sets of samples, the polarization resonant with our laser is y, with x-polarization being resonant at around 800 nm. For the following samples, the extinction spectra of the samples was strongly red-shifted, making the resonant polarization to be x, contrary to our expectations. This is quite surprising as the design parameters of the samples were very similar. Possible reasons for this shift are that the particles may have come out slightly thicker from the fabrication process or that there are some changes in the surface morphology of the particles, along the lines of Ref. [137].

The ρ^2-corrected SH yield was found to follow the same trend with respect to extinction resonance as it does for the particle size: the closer the extinction resonance is to the excitation wavelength, the better is SHG yield. However, this rule is not followed quite strictly. It is therefore possible that the coupling of the fields to the periodic grating slightly influences the nonlinear response.

The observations discussed in this section boil down to two conclusions: the extinction spectra can be fairly easily tuned to the desired wavelength in the visible–near IR region by tweaking the structural parameters of the samples. Changing the particle

size has a more pronounced effect on the extinction spectra than the particle separation and orientation. The SHG is enhanced when the excitation wavelength is close to the excitation resonance.

6.2 Chiral Symmetry Breaking

We found that our samples are extremely sensitive to the state of incident polarization and that they also modify it during the interaction. Our observations indicate that the small imperfections in the structures may break the assumed symmetry of the structures. This symmetry-breaking may render the structures chiral, which may be observed in both the linear and nonlinear responses.

Polarization Azimuth Rotation

In Paper 1 we hypothesized that the observed polarization azimuth rotation was a consequence of strong dichroism in the transmission. This means that at a given wavelength, one polarization is absorbed more strongly than the other. As the magnitude of one polarization component is reduced more than the other, their resultant appears rotated with respect to the original direction. This effect is called selective transmission and it is depicted in Fig. 6.3. In the figure we take also into account the possibility that the true principal axes of the system are rotated angle α with respect to the assumed principal axes. The eigenpolarizations and principal axes are still assumed linear and real, respectively.

Upon closer scrutiny, it was found that the assumed principal axes were not the true in-plane principal axes, and that the difference between the observed axes and the assumed principal axes exhibited a wavelength-dependence. Such dispersion of the axes is known to be possible in structures of very low symmetry [128], suggesting that our samples are also chiral.

For the purpose of analyzing the obtained PAR data, the previously-obtained dichroic transmission data was fitted to a model which describes the selective transmission, taking into account the possibility that the principal axes are rotated angle α with respect to the assumed principal axes x and y:

$$T = T_A \cos^2(\theta - \alpha) + T_B \sin^2(\theta - \alpha), \tag{6.2}$$

where T is the total transmittance, T_A and T_B are the transmittances along the new principal axes A and B, which are rotated angle α from the assumed x and y axes,

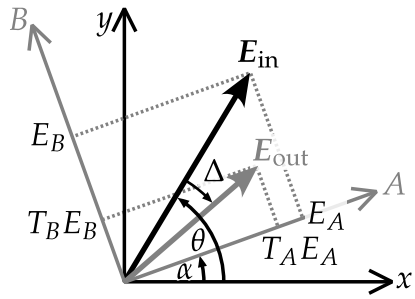

$$0 < T_A, T_B \leq 1$$

Figure 6.3 Selective transmission model.

cf. Fig. 6.3. Angle θ is the azimuth angle of the incident polarization, measured from the assumed x axis. In Paper 1 we observed a 7.6° shift at 1060 nm and at 820 nm the shift was already 11.5° [135], showing clear indication of dispersion.

Once the direction of the axes were established, we attempted to predict PAR data in terms of selective transmission:

$$\Delta = \arctan\left[\sqrt{\frac{T_B}{T_A}}\tan(\theta - \alpha)\right] - (\theta - \alpha). \tag{6.3}$$

However, selective transmission was not adequate to explain all results.

Optical Activity

Any deviations of the observed PAR data from model Eq. (6.3) is an implication of effects beyond in-plane anisotropy of the structure, such as chirality. Integrating Δ over all incident polarization directions removes the effect of anisotropy[138], so that when there is only dichroism, the net rotation should be zero.

Figure 6.4 presents experimentally determined dichroic transmission data and the corresponding polarization azimuth rotation data. The transmitted data has been fitted in terms of Eq. (6.2). The results of this fit have been used to predict the determined PAR. The results show that the cumulative azimuth rotation differs appreciably from zero, implying strongly that this particular sample is optically active, and indeed, chiral.

However, this is not the case for all of the samples. In Paper 1, the selective transmission model was adequate to explain the observed PAR, when the excitation wavelength was 1060 nm. The zero-crossings, or polarization directions with no detectable PAR, were at locations predicted by Eq. 6.3. On the other hand, at 820 nm, the model was unable to predict the experimental results and moreover, the separation of the

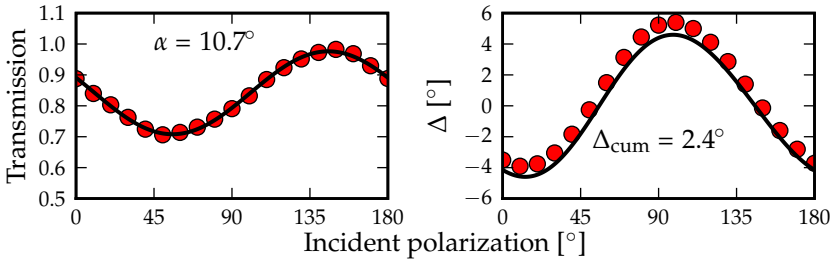

Figure 6.4 An example of a structure for which the selective transmission models fails to predict the observed polarization rotation. Previously unpublished data from an achiral structure. Left – Fit of Eq. (6.2) (solid line) to experimental data (circles). Right – prediction (solid line) of expected PAR by Eq. (6.3) and experimental PAR data (circles).

zero-crossings was found to be 102°. This result and the nonnegligible net PAR support the conclusion of optical activity at 820 nm[135], attributed to broken structural symmetry.

"Forbidden" SHG

The assumed symmetry of the L-structures allows us to derive a set of selection rules for the allowed polarization combinations of SHG. For structures in C_{1h} symmetry group, x-polarized SHG should only occur when the fundamental beam is purely x- or y-polarized. y-polarized SHG is possible only when then excitation has both x- and y-polarizations present.

We found in Papers 1–3, that for some of our structures the magnitude of the response is dominated by a symmetry-forbidden tensor component. For ideal L-shaped structures, even the tensor components arising from high-order interactions such as magnetic dipoles, electric quadrupoles etc. are symmetry-forbidden. Therefore, the source of these forbidden signals was symmetry-breaking, which lead us to investigate the chirality in our samples in more detail.

Circular-difference Response (CDR)

We continue the discussion of chirality in Paper 3, in which we designed structures to exhibit chirality on two levels: particle- and array-level [Fig. 5.3(b-d)]. Particle-level chirality was introduced by deliberately fabricating one arm of the L-structures 30% longer than the other arm, whereas the array-level chirality was achieved by rotating ideally symmetric structures 27° in their respective unit cells. For comparison, we

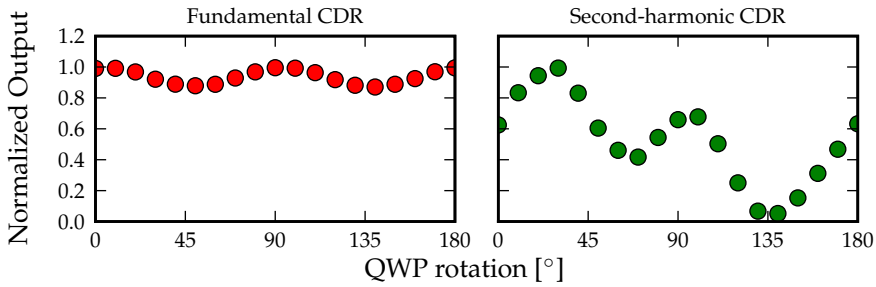

Figure 6.5 Experimental data for fundamental (left) and second-harmonic (right) circular-difference measurements. Data from Paper 3. This the data from the symmetric control sample. The excitation is right- and left-hand circularly polarized at 45° and 135°, respectively.

also fabricated symmetric structures in a symmetric lattice.

As chirality is expected to lead to different responses for left- and right-hand circularly polarized (LHC and RHC, respectively) light, a straightforward measure of the strength of chirality is the CDR. The difference in the intensities of responses under LHC and RHC excitation yields the expression for CDR[17,139]

$$\mathrm{CDR} = 2\frac{I_{\mathrm{LHC}} - I_{\mathrm{RHC}}}{I_{\mathrm{LHC}} + I_{\mathrm{RHC}}}, \tag{6.4}$$

which is valid for both fundamental and second-harmonic circular-difference responses. Experimental results for fundamental CDR show practically no difference in the transmitted signal for LHC and RHC (CDR $\sim$ 1 %, less than the experimental error), but second-harmonic CDR on the other hand, yields extraordinary results with responses on the order of $\sim$ 200% – even for the control array which was designed to be symmetric at both single particle and array levels.

This most remarkable result very strongly corroborates the interpretation that structural defects dominate the nonlinear responses, leaving the particle shape and mutual ordering in the array as secondary factors for this particular set of samples.

6.3 Multipolar Tensor Analysis

After we obtained evidence of chirality, we studied the origins of chirality in a more detailed level and how the chirality relates or leads to interactions beyond the electric-dipole approximation. Building the framework which enables us to describe the tensor aspect of second-harmonic generation without going into the (presently) as such inaccessible microscopic level, is the topic of Paper 4. We then proceeded to apply this formalism to our structures, discussed in detail in Papers 5 and 6.

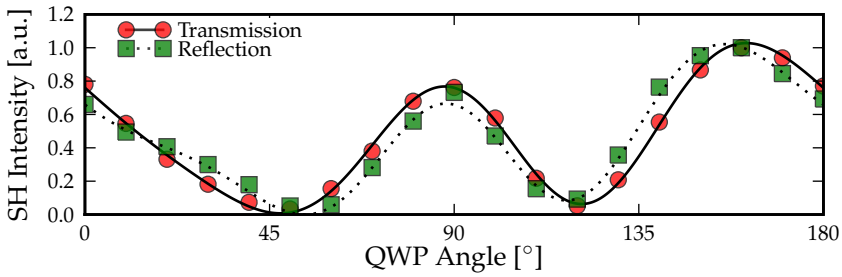

Figure 6.6 Example of measured lineshapes. Circles: transmission SH data; squares: reflection SH data. Solid and dashed lines are fits to the model function in transmission and reflection geometries, respectively. Data from Paper 6.

Multipoles

In Paper 5, we report direct evidence of the contribution of multipoles to the SH response. There we estimated multipoles to contribute up to 20% of the response. This exciting result inspired us to determine the full in-plane nonlinear response tensor, including the corresponding multipolar contributions to the tensor components.

We extracted the NRT components from the experimental data by employing the procedure described in Section 5.4. Figure 6.6 shows an example of the experimental data and the corresponding fit to the six in-plane NRT components. It can be immediately seen that the experimental data contains differences between the transmission and reflection arms, which already provides qualitative evidence of multipole contributions to the response.

To relate the NRT formalism to multipole effects, we again consider the transformation properties of different multipole sources as discussed in Section 4.4. The idea is further illustrated in Fig. 4.2 where we compare the radiated far fields of an electric dipole, a magnetic dipole, and an effective electric quadrupole. These differences in the radiative properties allow us to separate the different multipolar contributions to the response through comparison of the two signals.

To quantify the relative importance of different multipoles to the SH response, we separate each NRT component into symmetric and antisymmetric parts with respect to the choice of detection arm:

$$A_{ijk}^{\mathrm{T,R}} = A_{ijk}^{\mathrm{s}} \pm A_{ijk}^{\mathrm{as}}, \tag{6.5}$$

where superscripts "T" (+ sign) and "R" (− sign) refer to the transmitted and reflected directions and superscripts "s" and "as" refer to the symmetric and antisymmetric parts of the NRT, respectively. The symmetric part originates from the electric

dipole, whereas the antisymmetric part is attributed to magnetic-dipolar or electric-quadrupolar origins. We define the multipolar contribution γ of a given component as the ratio of the magnitudes of its antisymmetric and symmetric parts:

$$\gamma_{ijk} = \left| \frac{A^{\mathrm{as}}_{ijk}}{A^{\mathrm{s}}_{ijk}} \right|. \tag{6.6}$$

We have tabulated a summary of the results from fitting the nonlinear response tensor to our experimental data in Table 6.1. A more comprehensive tabulation can be found from Paper 6. The table shows that the largest component in magnitude, A_{yxx}, has also the largest absolute multipolar contribution. Moreover, this component should be zero by symmetry of an ideal L-shape. This suggests that the higher multipolar contributions are closely associated with chiral symmetry breaking of the sample.

A possible source of such symmetry breaking are asymmetrically distributed structural defects that remove the reflection symmetry of the sample with respect to the xz-plane. In Section 4.6 we proposed a phenomenological model in which the source of forbidden dipolar and quadrupolar SH signals was attributed to unevenly distributed structural defects.

This model however, is not limited to forbidden signals. Depending on the exact configuration of the SH sources, the defects may also give rise to other signals, possibly producing symmetry-allowed dipolar and quadrupolar signals.

Table 6.1. Summary of numerical results of simultaneous fits to experimental data, presenting the multipolar contributions of NRT components. Table summarizes those presented in Paper 6.

	Allowed	**Transmission**	**Reflection**	γ (%)
A_{xxx}	YES	1.00	1.00	0
A_{xyy}	YES	0.73	0.59	15
A_{xxy}	NO	0.23	0.18	20
A_{yxx}	NO	1.43	0.83	28
A_{yyy}	NO	0.13	0.20	21
A_{yxy}	YES	0.55	0.29	31

7 Conclusions and Outlook

To conclude, in this work we have studied linear and second-order nonlinear optical properties of L-shaped gold nanoparticles arranged in a regular array. These studies were begun with simple polarized spectral transmission studies in conjunction with SHG experiments. From these experiments, we found that SHG is greatly enhanced in the vicinity of plasmon resonances. Furthermore, we found that we can tune the resonances and thereby SHG with particle size, shape, and particle arrangement in the array. During the more detailed polarization studies on the linear and nonlinear responses of these nanoparticles we found that the details of the responses are due to defects of the samples. These defects may give rise to symmetry breaking and that way render ideally symmetric structures chiral. To study the role of these defects in even more detail, we developed a simple scattering-matrix type formalism with which to express the tensorial nature of SHG, without going into the microscopic details of the response. Using this formalism and relying on the spatial transformation properties of electric and magnetic dipoles and electric quadrupoles, we were able to determine the full in-plane SHG tensor and quantify the importance of higher multipoles to each tensor component. We found that a symmetry-forbidden component actually dominates the magnitude of the response and moreover, this component has the highest multipole contribution. To explain this behavior, we built a simple model where we assume that the symmetry is broken by surface defects on the nanoparticles. These defects give rise to the effective dipoles and quadrupoles in the total second-harmonic signal from that particular nanoparticle.

In the future, it would be exteremely interesting to address the role of multipoles in the fundamental wavelength. To do this, some changes to the response tensor formalism need to be made. It should be possible to derive symmetry arguments based on which the fundamental wavelength multipoles could be separated from SHG response. Furthermore, assessing the role of the surface quality of the nanoparticles on, first of all, SHG, and then on the details of SHG. This could be possibly achieved directly in the fabrication process by for instance annealing the nanoparticles. Also, the importance of higher multipoles needs to be studied under off-resonant excitation conditions.

On a more fundamental level, it will be important to address the microscopic origin of the second-order nonlinearity of metal nanostructures. Both surface effects and multipolar bulk effects can provide feasible mechanisms. The difficulty of separating

such effects goes back to the early days of nonlinear optics. However, our research group has developed techniques that allow certain parts of the surface and bulk effects to be separated.

In Chapter 1, we said that this project was begun with "several ideas and many open questions". Now, we have got some answers to our open questions, but during the process, a lot more open questions have come up. Nevertheless, increased understanding of the nonlinear properties of metal nanostructures is expected to lead to new materials with enhanced nonlinear responses.

Paljon on sarkaa vielä niitettävänä.

References

[1] B. K. Canfield, S. Kujala, K. Jefimovs, T. Vallius, J. Turunen, and M. Kauranen. Linear and Nonlinear Optical Responses Influenced by Broken Symmetry in an Array of Gold Nanoparticles. Opt. Express, **12**, 5418 (2004).

[2] B. K. Canfield, S. Kujala, K. Jefimovs, T. Vallius, J. Turunen, and M. Kauranen. Polarization Effects in the Linear and Nonlinear Optical Responses of Metal Nanoparticle Arrays. J. Opt. A: Pure Appl. Opt, **7**, S110 (2005).

[3] B. K. Canfield, S. Kujala, K. Laiho, K. Jefimovs, J. Turunen, and M. Kauranen. Chirality arising from small defects in gold nanoparticle arrays. Opt. Express, **14**, 950 (2006).

[4] B. K. Canfield, S. Kujala, K. Jefimovs, Y. Svirko, J. Turunen, and M. Kauranen. A macroscopic formalism to describe the second-order nonlinear optical response of nanostructures. J. Opt. A: Pure Appl. Opt, **8**, S278 (2006).

[5] S. Kujala, B. K. Canfield, M. Kauranen, Y. Svirko, and J. Turunen. Multipole Interference in the Second-Harmonic Optical Radiation from Gold Nanoparticles. Phys. Rev. Lett., **98**, 167403 (2007). Featured in April 30, 2007 issue of Virtual Journal of Nanoscale Science & Technology **15**, (2007).

[6] S. Kujala, B. K. Canfield, M. Kauranen, Y. Svirko, and J. Turunen. Multipolar analysis of second-harmonic radiation from gold nanoparticles. Opt. Express, **16**, 17196 (2008).

[7] C. F. Bohren and D. R. Huffman. *Absorption and Scattering of Light by Small Particles*. Wiley Science Paperback Series (Wiley, New York, 1998).

[8] Y. R. Shen. *The Principles of Nonlinear Optics* (John Wiley & Sons, Inc., 1984).

[9] J. Jackson. *Classical Electrodynamics* (John Wiley & Sons, Inc., 1975), 2nd edition.

[10] S. Cattaneo. *Two-beam Surface Second Harmonic Generation*. Ph.d., Tampere University of Technology (2004).

[11] R. W. Boyd. *Nonlinear Optics* (Academic Press, 2003), 2nd edition.

[12] G. P. Agrawal. *Nonlinear Fiber Optics* (Academic Press, 2001).

[13] C. A. Dailey, B. J. Burke, and G. J. Simpson. The general failure of Kleinman symmetry in practical nonlinear optical applications. Chem. Phys. Lett., **390**, 8 (2004).

[14] G. B. Arfken and H. J. Weber. *Mathematical Methods for Physicists* (Academic Press, 2001), 5th edition.

[15] M. Siltanen, E. Vuorimaa, H. Lemmetyinen, P. Ihalainen, J. Peltonen, and M. Kauranen. Nonlinear Optical and Structural Properties of Langmuir-Blodgett Films of Thiohelicenebisquinones. J. Phys. Chem. B, **112**, 1940 (2008).

[16] M. Kauranen, J. J. Maki, T. Verbiest, S. V. Elshocht, and A. Persoons. Quantitative determination of electric and magnetic second-order susceptibility tensors of chiral surfaces. Phys. Rev. B, **55**, R1985 (1997).

[17] J. J. Maki, M. Kauranen, and A. Persoons. Surface second-harmonic generation from

chiral materials. Phys. Rev. B, **51**, 1425 (1995).

[18] S. A. Maier. *Plasmonics: Fundamentals and Applications* (Springer, 2008).

[19] J. Reitz, F. Milford, and R. Christy. *Foundations of Electromagnetic Theory* (Addison-Wesley, 1993).

[20] H. Raether. *Surface Plasmons on Smooth and Rough Surfaces and on Gratings* (Springer, Berlin, 1988).

[21] K. L. Kelly, E. Coronado, L. L. Zhao, and G. C. Schatz. The Optical Properties of Metal Nanoparticles: The Influence of Size, Shape, and Dielectric Environment. J. Phys. Chem B, **107**, 668 (2003).

[22] U. Kreibig and M. Vollmer. *Optical Properties of Metal Clusters*. Springer Series in Materials Science (Springer, Berlin, 1995).

[23] G. Mie. Beiträge zur Optik trüber Medien, speziell kolloidaler Metallösungen. Ann. Phys., **25**, 377 (1908).

[24] C. F. Bohren and D. R. Huffman. *Absorption and Scattering of Light by Small Particles* (John Wiley & Sons, Inc., 1983).

[25] G. T. Boyd, T. Rasing, J. R. R. Leite, and Y. R. Shen. Local-field enhancement on rough surfaces of metals, semimetals, and semiconductors with the use of optical second-harmonic generation. Phys. Rev. B, **30**, 519 (1984).

[26] V. M. Shalaev, E. Y. Poliakov, and V. A. Markel. Small-particle composites. II. Nonlinear optical properties. Phys. Rev. B, **53**, 2437 (1996).

[27] L. Novotny. Effective Wavelength Scaling for Optical Antennas. Phys. Rev. Lett., **98**, 266802 (2007).

[28] W. Demtröder. *Laser Spectroscopy: Basic Concepts and Instrumentation* (Springer, 2003).

[29] M. Fleischmann, P. J. Hendra, and A. J. McQuillan. Raman spectra of pyridine adsorbed at a silver electrode. Chem. Phys. Lett., **26**, 163 (1974).

[30] B. J. Messinger, K. U. von Raben, R. K. Chang, and P. W. Barber. Local fields at the surface of noble-metal microspheres. Phys. Rev. B, **24**, 649 (1981).

[31] K. Kneipp, Y. Wang, H. Kneipp, L. T. Perelman, I. Itzkan, R. R. Dasari, and M. S. Feld. Single Molecule Detection Using Surface-Enhanced Raman Scattering (SERS). Phys. Rev. Lett., **78**, 1667 (1997).

[32] S. Nie and S. R. Emory. Probing Single Molecules and Single Nanoparticles by Surface-Enhanced Raman Scattering. Science, **275**, 1102 (1997).

[33] S. Zou and G. C. Schatz. Silver nanoparticle array structures that produce giant enhancements in electromagnetic fields. Chem. Phys. Lett., **403**, 62 (2005).

[34] Z. Zhou, G. Wang, and Z. Xu. Single-molecule detection in a liquid by surface-enhanced resonance Raman scattering. Appl. Phys. Lett., **88**, 034104 (2006).

[35] J. Zhang, Y. Fu, M. H. Chowdhury, and J. R. Lakowicz. Metal-Enhanced Single-Molecule Fluorescence on Silver Particle Monomer and Dimer: Coupling Effect between Metal Particles. Nano Lett., **7**, 2101 (2007).

[36] C. Chen, A. de Castro, and Y. Shen. Surface-Enhanced Second-Harmonic Generation. Phys. Rev. Lett., **46**, 145 (1981).

[37] C. K. Chen, T. F. Heinz, D. Ricard, and Y. R. Shen. Surface-enhanced second-harmonic generation and Raman scattering. Phys. Rev. B, **27**, 1965 (1983).

[38] L. H. Qian, X. Q. Yan, T. Fujita, A. Inoue, and M. W. Chena. Surface enhanced Raman scattering of nanoporous gold: Smaller pore sizes stronger enhancements. Appl. Phys. Lett., **90**, 153120 (2007).

[39] D. Ward, N. Grady, C. Levin, N. Halas, Y. Wu, P. Nordlander, and D. Natelson. Electromigrated Nanoscale Gaps for Surface-Enhanced Raman Spectroscopy. Nano Lett., **7**, 1396 (2007).

[40] J. B. Jackson, S. L. Westcott, L. R. Hirsch, J. L. West, and N. J. Halas. Controlling the surface enhanced Raman effect via the nanoshell geometry. Appl. Phys. Lett., **82**, 257 (2003).

[41] N. M. Perney, J. J. Baumberg, M. E. Zoorob, M. D. B. Charlton, S. Mahnkopf, and C. M. Netti. Tuning localized plasmons in nanostructured substrates for surface-enhanced Raman scattering. Opt. Express, **14**, 847 (2006).

[42] A. Amezcua-Correa, J. Yang, C. Finlayson, A. Peacock, J. Hayes, P. Sazio, J. Baumberg, and S. Howdle. Surface-enhanced Raman scattering using microstructured optical fiber substrates. Adv. Funct. Mater., **17**, 2024 (2007).

[43] J. Kneipp, X. Li, M. Sherwood, U. Panne, H. Kneipp, M. I. Stockman, and K. Kneipp. Gold Nanolenses Generated by Laser Ablation-Efficient Enhancing Structure for Surface Enhanced Raman Scattering Analytics and Sensing. Anal. Chem., **80**, 4247 (2008).

[44] E. Prodan, C. Radloff, N. J. Halas, and P. Nordlander. A Hybridization Model for the Plasmon Response of Complex Nanostructures. Science, **302**, 419 (2003).

[45] P. Nordlander, C. Oubre, E. Prodan, K. Li, and M. I. Stockman. Plasmon Hybridization in Nanoparticle Dimers. Nano Lett., **4**, 899 (2004).

[46] J. B. Lassiter, J. Aizpurua, L. I. Hernandez, D. W. Brandl, I. Romero, S. Lal, J. H. Hafner, P. Nordlander, and N. J. Halas. Close Encounters between Two Nanoshells. Nano Lett., **8**, 1212 (2008).

[47] D. P. Fromm, A. Sundaramurthy, P. J. Schuck, G. Kino, and W. E. Moerner. Gap-Dependent Optical Coupling of Single "Bowtie" Nanoantennas Resonant in the Visible. Nano Lett., **4**, 957 (2004).

[48] P. J. Schuck, D. P. Fromm, A. Sundaramurthy, G. S. Kino, and W. E. Moerner. Improving the Mismatch between Light and Nanoscale Objects with Gold Bowtie Nanoantennas. Phys. Rev. Lett., **94**, 017402 (2005).

[49] P. Mühlschlegel, H.-J. Eisler, O. J. F. Martin, B. Hecht, and D. W. Pohl. Resonant Optical Antennas. Science, **308**, 1607 (2005).

[50] K. Li, M. I. Stockman, and D. J. Bergman. Self-Similar Chain of Metal Nanospheres as an Efficient Nanolens. Phys. Rev. Lett., **91**, 227402 (2003).

[51] J. Dai, F. Cajko, I. Tsukerman, and M. I. Stockman. Electrodynamic effects in plasmonic nanolenses. Phys. Rev. B, **77**, 115419 (2008).

[52] S. J. Oldenburg, G. D. Hale, J. B. Jackson, and N. J. Halas. Light scattering from dipole and quadrupole nanoshell antennas. Appl. Phys. Lett., **75**, 1063 (1999).

[53] H. Wang, K. Fu, R. A. Drezek, and N. J. Halas. Light scattering from spherical plasmonic nanoantennas: effects of nanoscale roughness. Appl. Phys. B, **84**, 191 (2006).

[54] T. H. Taminiau, F. D. Stefani, F. B. Segerink, and N. F. van Hulst. Optical antennas direct single-molecule emission. Nat. Photon., **2**, 234 (2008).

[55] A. Alu and N. Engheta. Enhanced directivity from subwavelength infrared/optical nano-antennas loaded with plasmonic materials or metamaterials. IEEE T. Antenn.

Propag., **55**, 3027 (2007).

[56] H. F. Hofmann, T. Kosako, and Y. Kadoya. Design parameters for a nano-optical Yagi-Uda antenna. New J. Phys., **9**, 217 (2007).

[57] J. Li, A. Salandrino, and N. Engheta. Shaping light beams in the nanometer scale: A Yagi-Uda nanoantenna in the optical domain. Phys. Rev. B, **76**, 245403 (2007).

[58] N. Engheta. Circuits with Light at Nanoscales: Optical Nanocircuits Inspired by Metamaterials. Science, **317**, 1698 (2007).

[59] V. M. Shalaev. Optical negative-index metamaterials. Nat. Photon., **1**, 41 (2007).

[60] C. Enkrich, M. Wegener, S. Linden, S. Burger, L. Zschiedrich, F. Schmidt, J. F. Zhou, T. Koschny, and C. M. Soukoulis. Magnetic Metamaterials at Telecommunication and Visible Frequencies. Phys. Rev. Lett., **95**, 203901 (2005).

[61] V. Shalaev, W. Cai, U. Chettiar, H. Yuan, A. Sarychev, V. Drachev, and A. Kildishev. Negative index of refraction in optical metamaterials. Opt. Lett., **30**, 3356 (2005).

[62] T. Pakizeh, M. S. Abrishamian, N. Granpayeh, A. Dmitriev, and M. Käll. Magnetic-field enhancement in gold nanosandwiches. Opt. Express, **14**, 8240 (2006).

[63] M. W. Klein, C. Enkrich, M. Wegener, and S. Linden. Second-Harmonic Generation from Magnetic Metamaterials. Science, **313**, 502 (2006).

[64] M. W. Klein, M. Wegener, N. Feth, and S. Linden. Experiments on second- and third-harmonic generation from magnetic metamaterials. Opt. Express, **15**, 5238 (2007).

[65] L. D. Landau and E. Lifshitz. *Electrodynamics of Continuous Media*, volume 8 of *Course of Theoretical Physics* (Pergamon, 1960).

[66] E. U. Condon. Theories of Optical Rotatory Power. Rev. Mod. Phys., **9**, 432 (1937).

[67] P. Pershan. Nonlinear Optical Properties of Solids: Energy Considerations. Phys. Rev., **130**, 919 (1963).

[68] J. Zhou, L. Zhang, G. Tuttle, T. Koschny, and C. M. Soukoulis. Negative index materials using simple short wire pairs. Phys. Rev. B, **73**, 041101(R) (2006).

[69] S. Zhang, W. Fan, N. C. Panoiu, K. J. Malloy, R. M. Osgood, and S. R. J. Brueck. Experimental Demonstration of Near-Infrared Negative-Index Metamaterials. Phys. Rev. Lett., **95**, 137404 (2005).

[70] H. Schweizer, L. Fu, H. Gräbeldinger, H. Guo, N. Liu, S. Kaiser, and H. Giessen. Negative permeability around 630 nm in nanofabricated vertical meander metamaterials. Phys. Status Solidi A, **204**, 3886 (2007).

[71] U. Leonhardt. Optical Conformal Mapping. Science, **312**, 1777 (2006).

[72] J. B. Pendry, D. Schurig, and D. R. Smith. Controlling Electromagnetic Fields. Science, **312**, 1780 (2006).

[73] J. B. Pendry. Negative Refraction Makes a Perfect Lens. Phys. Rev. Lett., **85**, 3966 (2000).

[74] V. A. Fedotov, A. S. Schwanecke, N. I. Zheludev, V. V. Khardikov, and S. L. Prosvirnin. Asymmetric Transmission of Light and Enantiomerically Sensitive Plasmon Resonance in Planar Chiral Nanostructures. Nano Lett., **7**, 1996 (2007).

[75] H. Liu, D. A. Genov, D. M. Wu, Y. M. Liu, Z. W. Liu, C. Sun, S. N. Zhu, and X. Zhang. Magnetic plasmon hybridization and optical activity at optical frequencies in metallic nanostructures. Phys. Rev. B, **76**, 073101 (2007).

[76] N. Liu, H. Guo, L. Fu, S. Kaiser, H. Schweizer, and H. Giessen. Three-dimensional photonic metamaterials at optical frequencies. Nat. Mater., **7**, 31 (2008).

[77] J. Yao, Z. Liu, Y. Liu, Y. Wang, C. Sun, G. Bartal, A. M. Stacy, and X. Zhang. Optical Negative Refraction in Bulk Metamaterials of Nanowires. Science, **321**, 930 (2008).

[78] J. Valentine, S. Zhang, T. Zentgraf, E. Ulin-Avila, D. A. Genov, G. Bartal, and X. Zhang. Three-dimensional optical metamaterial with a negative refractive index. Nature, **455**, 376 (2008).

[79] N. W. Ashcroft and N. D. Mermin. *Solid State Physics* (Saunders College Publishing, 1976).

[80] V. M. Shalaev and A. K. Sarychev. Nonlinear optics of random metal-dielectric films. Phys. Rev. B, **57**, 13265 (1998).

[81] M. I. Stockman, S. V. Faleev, and D. J. Bergman. Coherent Control of Femtosecond Energy Localization in Nanosystems. Phys. Rev. Lett., **88**, 067402 (2002).

[82] M. I. Stockman, D. J. Bergman, C. Anceau, S. Brasselet, and J. Zyss. Enhanced Second-Harmonic Generation by Metal Surfaces with Nanoscale Roughness: Nanoscale Dephasing, Depolarization, and Correlations. Phys. Rev. Lett., **92**, 057402 (2004).

[83] K. Li, M. I. Stockman, and D. J. Bergman. Enhanced second harmonic generation in a self-similar chain of metal nanospheres. Phys. Rev. B, **72**, 153401 (2005).

[84] S. I. Bozhevolnyi, J. Beermann, and V. Coello. Direct Observation of Localized Second-Harmonic Enhancement in Random Metal Nanostructures. Phys. Rev. Lett., **90**, 197403 (2003).

[85] S. Takahashi and A. V. Zayats. Near-field second-harmonic generation at a metal tip apex. Appl. Phys. Lett., **80**, 3479 (2002).

[86] A. Bouhelier, M. Beversluis, A. Hartschuh, and L. Novotny. Near-Field Second-Harmonic Generation Induced by Local Field Enhancement. Phys. Rev. Lett., **90**, 013903 (2003).

[87] I. I. Smolyaninov, A. V. Zayats, and C. C. Davis. Near-field second harmonic generation from a rough metal surface. Phys. Rev. B, **56**, 9290 (1997).

[88] C. Anceau, S. Brasselet, J. Zyss, and P. Gadenne. Local second-harmonic generation enhancement on gold nanostructures probed by two-photon microscopy. Opt. Lett., **28**, 713 (2003).

[89] M. Zavelani-Rossi, M. Celebrano, P. Biagioni, D. Polli, M. Finazzi, L. Duò, G. Cerullo, M. Labardi, M. Allegrini, J. Grand, and P.-M. Adam. Near-field second-harmonic generation in single gold nanoparticles. Applied Physics Letters, **92**, 093119 (2008).

[90] B. Lamprecht, A. Leitner, and F. Aussenegg. Femtosecond decay-time measurement of electron-plasma oscillation in nanolithographically designed silver particles. Appl. Phys. B, **64**, 269 (1997).

[91] B. K. Canfield, H. Husu, J. Laukkanen, B. Bai, M. Kuittinen, J. Turunen, and M. Kauranen. Local Field Asymmetry Drives Second-Harmonic Generation in Noncentrosymmetric Nanodimers. Nano Lett., **7**, 1251 (2007).

[92] H. Husu, B. K. Canfield, J. Laukkanen, B. Bai, M. Kuittinen, J. Turunen, and M. Kauranen. Local-field effects in the nonlinear optical response of metamaterials. Metamat., **2**, 155 (2008).

[93] B. K. Canfield, H. Husu, J. Kontio, J. Viheriälä, T. Rytkönen, T. Niemi, E. Chandler, A. Hrin, J. A. Squier, and M. Kauranen. Inhomogeneities in the nonlinear tensorial re-

sponses of arrays of gold nanodots. New J. Phys., **10**, 013001 (2008).

[94] T. Y. F. Tsang. Surface-plasmon-enhanced third-harmonic generation in thin silver films. Opt. Lett., **21**, 245 (1996).

[95] A. V. Andreev, A. A. Korneev, L. S. Mukina, M. M. Nazarov, I. R. Prudnikov, and A. P. Shkurinov. Simultaneous generation of second and third optical harmonics on a metal grating. Phys. Rev. B, **74**, 235421 (2006).

[96] M. Danckwerts and L. Novotny. Optical Frequency Mixing at Coupled Gold Nanoparticles. Phys. Rev. Lett., **98**, 026104 (2007).

[97] S. Palomba and L. Novotny. Nonlinear Excitation of Surface Plasmon Polaritons by Four-Wave Mixing. Phys. Rev. Lett., **101**, 056802 (2008).

[98] T. W. Ebbesen, H. J. Lezec, H. F. Ghaemi, T. Thio, and P. A.Wolff. Extraordinary optical transmission through sub-wavelength hole arrays. Nature, **391**, 667 (1998).

[99] P. Lalanne, J. C. Rodier, and J. P. Hugonin. Surface plasmons of metallic surfaces perforated by nanohole arrays. J. Opt. A: Pure Appl. Opt, **7**, 422 (2005).

[100] A. Nahata, R. A. Linke, T. Ishi, and K. Ohashi. Enhanced nonlinear optical conversion from a periodically nanostructured metal film. Opt. Lett., **28**, 423 (2003).

[101] M. Airola, Y. Liu, and S. Blair. Second-harmonic generation from an array of sub-wavelength metal apertures. J. Opt. A: Pure Appl. Opt, **7**, 118 (2005).

[102] A. Lesuffleur, L. K. S. Kumar, and R. Gordon. Enhanced second harmonic generation from nanoscale double-hole arrays in a gold film. Appl. Phys. Lett., **88**, 261104 (2006).

[103] N. Feth, S. Linden, M. W. Klein, M. Decker, F. B. P. Niesler, Y. Zeng, W. Hoyer, J. Liu, S. W. Koch, J. V. Moloney, and M. Wegener. Second-harmonic generation from complementary split-ring resonators. Opt. Lett., **33**, 1975 (2008).

[104] P. Guyot-Sionnest, W. Chen, and Y. Shen. General considerations on optical second-harmonic generation from surfaces and interfaces. Phys. Rev. B, **33**, 8254 (1986).

[105] J. Krenn, G. Schider, W. Rechberger, B. Lamprecht, F. Leitner, A. Aussenegg, and J. Weeber. Design of multipolar plasmon excitations in silver nanoparticles. Appl. Phys. Lett., **77**, 3379 (2000).

[106] U. Kreibig, B. Schmitz, and H. D. Breuer. Separation of plasmon-polariton modes of small metal particles. Phys. Rev. B, **36**, 5027 (1987).

[107] S. Malynych and G. Chumanov. Light-Induced Coherent Interactions between Silver Nanoparticles in Two-Dimensional Arrays. J. Am. Chem. Soc., **125**, 2896 (2003).

[108] L. Gunnarsson, T. Rindzevicius, J. Prikulis, B. Kasemo, M. Käll, S. Zou, and G. C. Schatz. Confined Plasmons in Nanofabricated Single Silver Particle Pairs: Experimental Observations of Strong Interparticle Interactions. J. Phys. Chem. B, **109**, 1079 (2005).

[109] J. E. Millstone, S. Park, K. L. Shuford, L. D. Qin, G. C. Schatz, and C. A. Mirkin. Observation of a quadrupole plasmon mode for a colloidal solution of gold nanoprisms. J. Am. Chem. Soc., **127**, 5312 (2005).

[110] K. L. Shuford, M. A. Ratner, and G. C. Schatz. Multipolar excitation in triangular nanoprisms. J. Chem. Phys., **123**, 114713 (2005).

[111] R. Bukasov and J. S. Shumaker-Parry. Highly Tunable Infrared Extinction Properties of Gold Nanocrescents. Nano Lett., **7**, 1113 (2007).

[112] A. K. Sheridan, A. W. Clark, A. Glidle, J. M. Cooper, and D. R. S. Cumming. Multiple plasmon resonances from gold nanostructures. Appl. Phys. Lett., **90**, 143105 (2007).

[113] T. Uwada, T. Asahi, H. Masuhara, D. Ibano, M. Fujishiro, and T. Tominaga. Multipole resonance modes in localized surface plasmon of single hexagonal/triangular gold nanoplates. CHEMISTRY LETTERS, **36**, 318 (2007).

[114] N. Felidj, J. Grand, G. Laurent, J. Aubard, G. Levi, A. Hohenau, N. Galler, F. R. Aussenegg, and J. R. Krenn. Multipolar surface plasmon peaks on gold nanotriangles. J. Chem. Phys., **128**, 094702 (2008).

[115] R. Esteban, R. Vogelgesang, J. Dorfmüller, A. Dmitriev, C. Rockstuhl, C. Etrich, and K. Kern. Direct Near-Field Optical Imaging of Higher Order Plasmonic Resonances. Nano Lett., **XX**, DOI:10.1021/nl801396r (2008).

[116] M. Rang, A. C. Jones, F. Zhou, Z.-Y. Li, B. J. Wiley, Y. Xia, and M. B. Raschke. Optical Near-Field Mapping of Plasmonic Nanoprisms. Nano Lett., **XX**, DOI:10.1021/nl801808b (2008).

[117] G. Laurent, N. Félidj, J. Aubard, G. Lévi, J. R. Krenn, A. Hohenau, G. Schider, A. Leitner, and F. R. Aussenegg. Evidence of multipolar excitations in surface enhanced Raman scattering. Phys. Rev. B, **71**, 045430 (2005).

[118] V. L. Brudny, W. L. Mochán, J. A. Maytorena, and B. S. Mendoza. Second harmonic generation from a collection of nanoparticles. Phys. Status Solidi B, **240**, 518 (2003).

[119] J. I. Dadap, J. Shan, and T. F. Heinz. Theory of optical second-harmonic generation from a sphere of centrosymmetric material: small-particle limit. J. Opt. Soc. Am. B, **21**, 1328 (2004).

[120] J. Nappa, G. Revillod, I. Russier-Antoine, E. Benichou, C. Jonin, and P. F. Brevet. Electric dipole origin of the second harmonic generation of small metallic particles. Phys. Rev. B, **71**, 165407 (2005).

[121] J. Nappa, I. Russier-Antoine, E. Benichou, C. Jonin, and P. F. Brevet. Second harmonic generation from small gold metallic particles: From the dipolar to the quadrupolar response. J. Chem. Phys., **125**, 184712 (2006).

[122] A. Moran, J. Sung, E. Hicks, R. Van Duyne, and K. Spears. Second harmonic excitation spectroscopy of silver nanoparticle arrays. J. Phys. Chem. B, **109**, 4501 (2005).

[123] I. Russier-Antoine, E. Benichou, G. Bachelier, C. Jonin, and P. Brevet. Multipolar contributions of the second harmonic generation from silver and gold nanoparticles. J. Phys. Chem. C, **111**, 9044 (2007).

[124] L. Cao, N. C. Panoiu, and R. M. J. Osgood. Surface second-harmonic generation from surface plasmon waves scattered by metallic nanostructures. Phys. Rev. B, **75**, 205401 (2007).

[125] M. Finazzi, P. Biagioni, M. Celebrano, and L. Duò. Selection rules for second-harmonic generation in nanoparticles. Phys. Rev. B, **76**, 125414 (2007).

[126] G. Bachelier, I. Russier-Antoine, E. Benichou, C. Jonin, and P.-F. Brevet. Multipolar second-harmonic generation in noble metal nanoparticles. J. Opt. Soc. Am. B, **25**, 955 (2008).

[127] W. K. H. Panofsky and M. Phillips. *Classical Electricity and Magnetism* (Addison-Wesley, 1962), 2nd edition.

[128] M. Born and E. Wolf. *Principles of Optics* (Cambridge University Press, 1999), 7th edition.

[129] J. I. Dadap, J. Shan, K. B. Eisenthal, and T. F. Heinz. Second-Harmonic Rayleigh Scattering from a Sphere of Centrosymmetric Material. Phys. Rev. Lett., **83**, 4045 (1999).

[130] J. Nappa, I. Russier-Antoine, E. Benichou, C. Jonin, and P.-F. Brevet. Wavelength depen-

dence of the retardation effects in silver nanoparticles followed by polarization resolved hyper Rayleigh scattering. Chem. Phys. Lett., **415**, 246 (2005).

[131] L. Novotny and B. Hecht. *Principles of Nano-optics* (Cambridge University Press, New York, 2007).

[132] E. Adler. Nonlinear Optical Frequency Polarization in a Dielectric. Phys. Rev., **134**, A728 (1964).

[133] D. Epperlein, B. Dick, G. Marowsky, and G. Reider. Second-harmonic generation in centro-symmetric media. Appl. Phys. B, **44**, 5 (1987).

[134] H. Tuovinen, M. Kauranen, K. Jefimovs, P. Vahimaa, T. Vallius, J. Turunen, N. V. Tkachenko, and H. Lemmetyinen. Linear and second-order nonlinear optical properties of arrays of noncentrosymmetric gold nanoparticles. J. Nonlinear Opt. Phys., **11**, 421 (2002).

[135] B. K. Canfield, S. Kujala, K. Jefimovs, T. Vallius, J. Turunen, and M. Kauranen. Remarkable Polarization Sensitivity of Gold Nanoparticle Arrays. Appl. Phys. Lett., **86**, 183109 (2005).

[136] F. X. Wang, M. Siltanen, and M. Kauranen. Uniqueness of determination of second-order nonlinear optical expansion coefficients of thin films. Phys. Rev. B, **76**, 085428 (2007).

[137] Y. S. Jung, Z. Sun, H. K. Kima, and J. Blachere. Blueshift of surface plasmon resonance spectra in anneal-treated silver nanoslit arrays. Appl. Phys. Lett., **87**, 263116 (2005).

[138] T. Vallius, K. Jefimovs, J. Turunen, P. Vahimaa, and Y. Svirko. Optical activity in subwavelength-period arrays of chiral metallic particles. Appl. Phys. Lett., **83**, 234 (2003).

[139] M. Kauranen, T. Verbiest, S. V. Elshocht, and A. Persoons. Chirality in surface nonlinear optics. Opt. Mater., **9**, 286 (1998).

Appendices

Paper 1

Brian K. Canfield, Sami Kujala, Konstantins Jefimovs,
Jari Turunen, and Martti Kauranen.

Linear and nonlinear optical responses influenced by broken symmetry in an array of gold nanoparticles.

Optics Express **12**, 5418 (2004).

Paper 2

Brian K. Canfield, Sami Kujala, Konstantins Jefimovs,
Tuomas Vallius, Jari Turunen, and Martti Kauranen.

Polarization effects in the linear and nonlinear optical responses of gold nanoparticle arrays.

Journal of Optics A: Pure and Applied Optics **7**, S110 (2005).

Paper 3

Brian K. Canfield, Sami Kujala, Kaisa Laiho, Konstantins Jefimovs,
Jari Turunen, and Martti Kauranen,

Chirality arising from small defects in gold nanoparticle arrays

Opt. Express **14**, 950 (2006)

Paper 4

Brian K. Canfield, Sami Kujala, Konstantins Jefimovs,
Yuri Svirko, Jari Turunen, and Martti Kauranen

A macroscopic formalism to describe the second-order nonlinear optical response of nanostructures

J. Opt. A: Pure Appl. Opt **8**, S278 (2006)

Paper 5

Sami Kujala, Brian K. Canfield, Martti Kauranen,
Yuri Svirko, and Jari Turunen

*Multipole Interference in the Second-Harmonic
Optical Radiation from Gold Nanoparticles*

Phys. Rev. Lett. **98**, 167403 (2007), featured in April 30, 2007 issue of
Virtual Journal of Nanoscale Science & Technology **15**, (2007).

Paper 6

Sami Kujala, Brian K. Canfield, Martti Kauranen,
Yuri Svirko, and Jari Turunen

Multipolar analysis of second-harmonic radiation from gold nanoparticles

Opt. Express, **16**, 17196 (2008).